



# Applications and limitations of constrained high-resolution peak fitting on low resolving power mass spectra from the ToF-ACSM

Hilkka Timonen<sup>1</sup>, Mike Cubison<sup>2</sup>, Minna Aurela<sup>1</sup>, David Brus<sup>1</sup>, Heikki Lihavainen<sup>1</sup>, Risto Hillamo<sup>1</sup>, Manjula Canagaratna<sup>3</sup>, Bettina Nekat<sup>4</sup>, Rolf Weller<sup>3</sup>, Douglas Worsnop<sup>3</sup>, and Sanna Saarikoski<sup>1</sup>

<sup>1</sup>Atmospheric composition research, Finnish Meteorological Institute, Helsinki, Finland

<sup>2</sup>TOFWERK AG, Thun, Switzerland

<sup>3</sup>Aerodyne Research Inc., Billerica, MA, USA

<sup>4</sup>The Alfred Wegener Institute, Helmholtz Centre for Polar and Marine Research, Bremerhaven, Germany

Correspondence to: Hilkka Timonen (hilkka.timonen@fmi.fi)

Received: 15 January 2016 – Published in Atmos. Meas. Tech. Discuss.: 2 March 2016

Revised: 31 May 2016 – Accepted: 22 June 2016 – Published: 25 July 2016

**Abstract.** The applicability, methods and limitations of constrained peak fitting on mass spectra of low mass resolving power ( $m/\Delta m_{50} \sim 500$ ) recorded with a time-of-flight aerosol chemical speciation monitor (ToF-ACSM) are explored. Calibration measurements as well as ambient data are used to exemplify the methods that should be applied to maximise data quality and assess confidence in peak-fitting results. Sensitivity analyses and basic peak fit metrics such as normalised ion separation are employed to demonstrate which peak-fitting analyses commonly performed in high-resolution aerosol mass spectrometry are appropriate to perform on spectra of this resolving power. Information on aerosol sulfate, nitrate, sodium chloride, methanesulfonic acid as well as semi-volatile metal species retrieved from these methods is evaluated. The constants in a commonly used formula for the estimation of the mass concentration of hydrocarbon-like organic aerosol may be refined based on peak-fitting results. Finally, application of a recently published parameterisation for the estimation of carbon oxidation state to ToF-ACSM spectra is validated for a range of organic standards and its use demonstrated for ambient urban data.

## 1 Introduction

Atmospheric aerosols influence health, climate and visibility (Pope and Dockery, 2006; IPCC, 2013). All these influences are tightly linked with particulate matter (PM) concen-

tration and PM chemical composition (IPCC, 2013). Traditionally, aerosol composition was studied by collecting particulate matter on a filter substrate for an extended period ranging from hours to days and subsequent composition analysis in laboratory. Development of online analysis instruments, particularly based on aerosol mass spectrometry, has enabled the measurement of chemical composition of PM in real time. The Aerodyne aerosol mass spectrometer (AMS; Jayne et al., 2000; DeCarlo et al., 2006) is designed to provide detailed information on size-resolved aerosol chemical composition for short- to medium-term campaigns (weeks to months); however, it is not suitable for long-term monitoring without the presence of an operator. The Aerodyne aerosol chemical speciation monitor (Q-ACSM; Ng et al., 2011b) is based on AMS technology but adapted for long-term monitoring; however, the quadrupole detector limits the mass resolving power to unity and provides reduced sensitivity compared with the AMS. A recently developed version of this instrument employing time-of-flight (ToF) detection provides greater sensitivity and mass resolving power of around 500 (ToF-ACSM; Fröhlich et al., 2013). Whilst the increase in sensitivity relative to the Q-ACSM is an obvious advantage for measurements in clean locations such as Antarctica or for increasing temporal resolution, the limits of potential extra information afforded by the increased mass resolving power, and in particular the associated uncertainties on peak-fitting parameters, are as yet unexplored in literature.

In analysis of high-resolution AMS data, peak fitting is typically employed to retrieve signal intensities of ions

whose peaks overlap in the mass spectrum, expanding greatly the content and quality of information that may be extracted from the data in comparison to simple peak integration (e.g. DeCarlo et al., 2006; Aiken et al., 2008). Fröhlich et al. (2013) demonstrated that peak fitting could be applied to ToF-ACSM data and presented a simple example for a single isobaric peak, but the extent and limitations of the applicability of the technique were not explored. This paper addresses the question of what extra information can be obtained by fitting the MS peaks. Recently, the uncertainty on fitted peak intensity associated with the constrained peak-fitting procedure employed by the AMS community has been explored and parameterisations for calculation of the precision reported (Corbin et al., 2015; Cubison and Jimenez, 2015). These are used, together with the appropriate sensitivity analyses, to assess the confidence in the peak-fitting results and draw conclusions on the appropriateness of applying peak fitting for retrieval of overlapping ion peak intensities for a range of example scenarios measured with a ToF-ACSM.

## 2 Experimental

### 2.1 Time-of-flight aerosol chemical speciation monitor

The ToF-ACSM (Fröhlich et al., 2013; Aerodyne Research Inc., Billerica, USA) is designed for long-term monitoring of submicron aerosol composition with temporal resolution of typically 10 min (and up to 1 Hz) and mass resolving power  $m/\Delta m_{50}$  of typically 500 (and up to 600). Based on the sampling technology of the ToF-AMS (time-of-flight aerosol mass spectrometer; Drewnick et al., 2005; DeCarlo et al., 2006), the ToF-ACSM contains a critical orifice to constrain the flow ( $1.4 \text{ cm}^3 \text{ s}^{-1}$ ) and an aerodynamic lens to focus submicron particles into a narrow beam introduced into a differentially pumped vacuum chamber where the gas molecules tend to diverge from the beam path and are pumped away, concentrating the aerosol: gas molecule ratio by a factor of around  $10^7$ . The particle beam impacts a heated plate held at  $600^\circ\text{C}$  and the molecules are vaporised and immediately ionised using 70 eV electron impact (EI) ionisation. The ions are introduced into a compact time-of-flight mass analyser (ETOF, TOFWERK AG, Thun, Switzerland) and extracted orthogonally using pulsed extraction for eventual detection with a discrete dynode detector. Mass spectra are recorded with and without the use of a filter in the inlet line; the resulting difference in recorded signal is prescribed to the aerosol. These signals are converted to nitrate equivalent mass concentrations using the same ionisation efficiency calibration procedure utilised for the AMS and described by Jimenez et al. (2003). Post-processing was performed using the data analysis package “Tofware” (version 2.5.3, [www.tofwerk.com/tofware](http://www.tofwerk.com/tofware)) running in the Igor Pro (Wavemetrics, OR, USA) environment.

### 2.2 Measurement locations and datasets

Three ToF-ACSM datasets were used to study the applicability and limitations of constrained peak fitting on mass spectra recorded with the ToF-ACSM, measured in clean background conditions (Neumayer, Antarctica), in the urban background (SMEAR III) and in an industrial environment (underground mine, Kemi).

#### 2.2.1 Helsinki, Finland

ToF-ACSM measurements were conducted at the SMEAR III measurement station in Helsinki, Finland, from 2 to 8 March 2014. The SMEAR III station (Station for Measuring Ecosystem–Atmosphere Relationships;  $60^\circ 12' \text{ N}$ ,  $24^\circ 57' \text{ E}$ ; 30 m a.s.l.; Järvi et al., 2009) is an urban background measurement station for the long-term measurement and investigation of chemical and physical properties of atmospheric aerosols and trace gases, meteorological parameters and turbulent fluxes. The station is situated on the Kumpula campus, 5 km northeast from the centre of Helsinki. Approx. 200 m east of the station is a major road with heavy traffic ( $60\,000 \text{ cars day}^{-1}$ ). A collection efficiency of 0.5 was assumed based on previous studies conducted on SMEAR III station, e.g. Aurela et al. (2015). During the measurement period presented here the PM concentrations exhibited a mean average of  $16.2 \mu\text{g m}^{-3}$ . However, larger concentrations up to  $45 \mu\text{g m}^{-3}$  were observed (Fig. S1).

#### 2.2.2 Antarctica

ToF-ACSM measurements were conducted at the Neumayer III station in Antarctica ( $70.6744^\circ \text{ S}$ ,  $8.2742^\circ \text{ W}$ ; [http://www.awi.de/en/go/air\\_chemistry\\_observatory](http://www.awi.de/en/go/air_chemistry_observatory); Weller et al., 2011) during the Antarctic summer from December 2014 to February 2015. Located far from primary emission sources, the Neumayer III station is an ideal location for conducting background measurements free from anthropogenic influences (Weller et al., 2015). The two most frequently observed classes of aerosol observed in Antarctica contain sulfur and sea salt. Sulfur-containing particles, whose secondary production in the atmosphere is controlled by pathways including photochemical reactions involving dimethyl sulfide emitted by the oceans, dominate particle number concentrations in the Antarctic atmosphere most of the time (Korhonen et al., 2008; Weller et al., 2011).

Very low background aerosol concentrations of less than  $1 \mu\text{g m}^{-3}$  were typically measured, consisting almost purely of sulfate and chloride compounds. Larger PM concentrations were observed during January and February (up to  $3 \mu\text{g m}^{-3}$ ) when the temperature was higher and the adjacent ocean ice free. We have chosen two distinct episodes for use in analyses presented in this work. Each exhibited different characteristics and posed different problems for extracting information from the data using peak fitting. Episode 1 (2–

3 December 2014) represents emissions from sea areas and had elevated chloride concentrations. During episode 2 (7–13 January 2015) elevated sulfate and methanesulfonic acid (MSA) concentrations were observed.

### 2.2.3 Underground mine

ToF-ACSM measurements were conducted at the Kemi Mine (Outokumpu Chrome Oy) 500 m below the surface during the spring of 2014 as a part of a project aiming to help development of a sustainable and safe mining environment. The main sources of particles in the underground mine were the ore extraction and processing for coarse particles and diesel exhausts from mining machinery and transport vehicles for submicron particles. A subset of the data is used here in order to test peak fitting on information-rich mass spectra taken in an environment with high PM concentrations.

## 3 Methods

### 3.1 Peak-fitting methodology

The post-processing software “Tofware” utilised for ToF-ACSM analysis uses a peak deconvolution routine where the peak positions are defined a priori and held fixed in the fitting procedure, based on the methodology utilised by the PIKA software of the ToF-AMS community (DeCarlo et al., 2006; Sueper, 2008). EI ionisation, as is used in the ToF-ACSM, tends to ionise and fragment the molecules in a very consistent manner. Thus, 1 degree of freedom is removed from the ion fitting procedure, which can be based upon a comprehensive list of ions and their exact  $m/Q$  that define the fitted centroid values. Furthermore, the peak model (width and shape) is held fixed for a given isobaric mass and the mass calibration is also defined a priori and held constant. The only parameter to vary is thus peak intensity, for which the optimal values for all peaks at a given isobar are ascertained by non-negative least-squares optimisation using the active set method of Lawson and Hanson (1995). We present here a detailed description of each step in the setup of the peak-fitting routine, with exception of the mass calibration, which is discussed at length in the following section.

#### 3.1.1 Mass spectral baseline subtraction

Mass spectra recorded using analogue-to-digital converters to digitise the detector signal for data acquisition purposes, as is the case in the ToF-ACSM, can be expected to exhibit a non-zero mass spectral baseline as a result of background ions and, potentially, electronic noise (Fig. 1). In addition, peaks adjacent to large signals (such as  $N_2^+$  in the ToF-ACSM) can be expected to be superimposed upon a significant baseline varying in intensity with  $m/Q$ . It is important to subtract this baseline from the mass spectrum before carrying out the peak fit procedure. As it is desired to let the

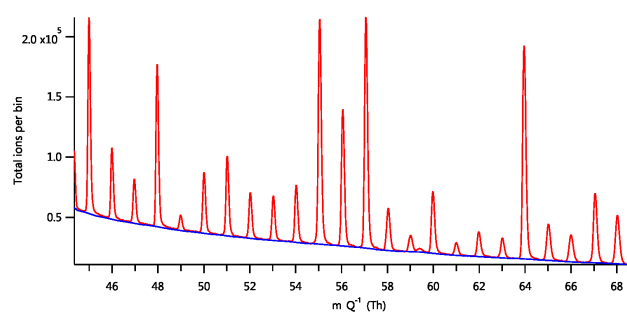


**Figure 1.** Example of a mass spectral baseline determined using the methodology described in the text.

analysis software execute peak fitting as a batch process upon large numbers of mass spectra, a parameterisation is required which can reliably generate the MS baseline based on only a few tuneable parameters. Tofware achieves this through a simple two-step process:

- i. a low-pass filter is applied to the MS to remove noise;
- ii. a running box average of the de-noised MS is generated based not on the mean but on the lowest data point in the box.

Provided the box width is set large enough such that it extends over the entire width of a typical MS peak, step (ii) effectively interpolates over the peaks as it takes the lowest data point at each step. Step (i) has the effect of ensuring the calculated baseline tends to run through the centre and not along the bottom edge of the noise. By default, the width of the box is set to 40 mass spectral data points (50 ns). It is possible that, in regions adjacent to large peaks with significant gradients, the box method generates a baseline slightly lower than the optimum. However, the peak most significantly impacted by this effect,  $NO^+$ , the negative offset is observed to be at most 5 % of peak height and typically lower. This offset is also removed during calculation of the difference spectrum, although it does contribute to a slightly higher imprecision. The low-pass filter (Zahradník and Vlcek, 2004) used in step (i) removes by default frequencies higher than 16 GHz. We note that sometimes the baseline might not be reached between large peaks, especially at higher  $m/Q$  range. For ToF-ACSM mass range (up to  $m/Q \sim 200$ ) this is, however, not an issue.

#### 3.1.2 Determination of instrumental transfer function (peak model)

##### Peak width

The width of an isolated ion peak is expected to observe a linear relationship with  $m/Q$ . A scatter plot of peak width vs.  $m/Q$  for isolated ions will thus highlight MS peaks that represent multiple, overlapping, ions as they will lie above the

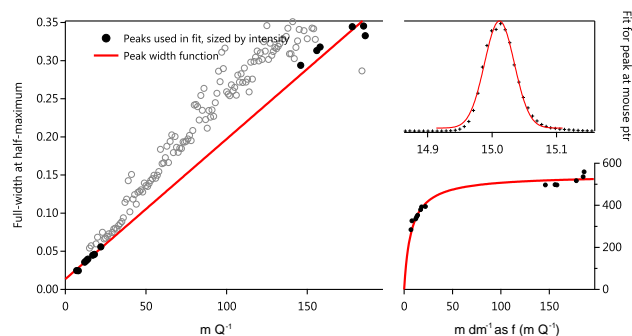


**Figure 2.** Ascertaining the peak width as a function of  $m/Q$ : the straight-line fit (peak width function, in red) is applied to the chosen data points (in black), giving the relationship for mass resolving power shown bottom-right. The principle behind this methodology is that isolated ions (in black) should exhibit narrower peak widths than those with adjacent ions (in grey).

linear regression line (Meija and Caruso, 2004) as shown in Fig. 2. Junninen et al. (2010) and Stark et al. (2015) both used this effect to develop peak width parameterisations for use in atmospheric science analysis software; an adapted version of the method of Stark et al. (2015) is utilised here. Müller et al. (2013) report on a robust method for peak width calculation in proton mass-transfer mass spectrometry which utilises the same list of known isolated ions as the mass calibration. A similar method could certainly be employed for the lower part of the ToF-ACSM mass spectrum but would require extrapolation to high  $m/Q$ . To constrain the upper end of the linear regression, the following steps are taken:

- i. the  $N$  most intense peaks in the spectrum are found, where  $N$  is the largest  $m/Q$  measured divided by 3;
- ii. a single Gaussian is fitted to each MS peak;
- iii. a straight-line fit is applied to the scatter plot of full width at half maximum vs.  $m/Q$ ;
- iv. step (iii) is iterated, removing the point that lies the furthest above the fit line, until 10 peaks remain.

The user may choose additional peaks to use at step (iv), and has the option to manually remove any points from the linear fit of step (iii). Peak width is not expected to vary greatly over time other than with changes in instrument tuning. Thus the default peak width is calculated automatically for each 24 h data file, but the user can define a revised version, typically once for each set of instrument tuning parameters during an experimental campaign, and save this in the data files for future use.

### Peak shape

Owing foremost to the energetic primary ion beam, the measured shape of the ion peaks in the ToF-ACSM mass spec-

trum is often distinctly non-Gaussian and not easily described using mathematical functions. Therefore, rather than attempt to reduce the observed shape to a combination of functions, each peak is represented with a custom peak shape function following the high-resolution time-of-flight aerosol mass spectrometer (HR-ToF-AMS) methodology proposed by DeCarlo et al. (2006) and adapted for use in multiple atmospheric science analysis packages (Sueper, 2008; Junninen et al., 2010; Müller et al., 2013; Stark et al., 2015). The ToF-ACSM peak shape is determined using the following routine:

- i. the 20 largest peaks in the spectrum are found and a single Gaussian fitted to each;
- ii. the measured shape of the peak is normalised to the fitted Gaussian width;
- iii. the second derivative of each normalised peak is analysed and peaks with shoulders are discarded (Fig. S2);
- iv. all the remaining normalised shapes are averaged to generate the custom peak shape.

The user may additionally choose to fit more/fewer peaks at step (i) and has the option to apply additional constraints such as monotonicity and thresholds on the min/max ion counts. The custom peak shape is typically defined once for each set of instrument tuning parameters during an experimental campaign and is saved in the data files for future use.

The assumption of consistent peak shape has been widely employed in the atmospheric community (e.g. Cappellin et al., 2011); nonetheless this does not prove its validity. Note that this is not the case for ions that do not originate in the source plume, such as  $K^+$  ions stemming from surface ionisation on the ToF-ACSM heater. User error – i.e. an incorrect definition of peak shape – is also a potential source of error and arguably of greater probability and magnitude than any potential instrumental artefacts. A comprehensive study of the impact of a varying or incorrectly determined peak shape would be a useful addition to the literature. However, to highlight the validity of the invariant peak shape assumption for this study, we (i) verified that the peak shape was invariant over a large mass range by comparing the shape for known isolated ions in a calibration measurement where  $SF_6$  gas was injected at the ioniser (see Fig. S3) and (ii) verified that the peak shape was invariant over time by comparing the shape of the  $N_2^+$  peak for nearly a month of data (Fig. S4).

### 3.1.3 Peak list

For HR-ToF-AMS data, the list of ion peaks to be utilised during peak fitting has been assembled and extended over a decade of instrument development and is quite comprehensive in nature (Sueper, 2008). Most of these ions are, however, unresolvable with the mass resolving power of the

ETOFS-equipped ToF-ACSM, which precludes use of the HR-ToF-AMS ion list. The particular ions to fit must therefore be carefully considered based on targeted analyses, rather than taking the blanket approach of fitting everything. In the results section we present multiple case studies highlighting the state-of-the-art knowledge of which ions/ion groups are appropriate for inclusion in peak-fitting analyses of ToF-ACSM data.

### 3.2 Mass calibration

ToF-ACSM measurement profiles are typically converted from time-of-flight to mass-to-charge space and vice versa using the numerical relationship  $\text{ToF} = a + b \times \sqrt{(m/Q)}$ , where  $a$  and  $b$  are constants. In the constrained peak-fitting procedure employed during ToF-ACSM and AMS analysis, the accuracy and precision of the mass calibration are of critical importance, because the fitting is performed in time-of-flight space and the position of the fitted peaks held constant using fixed mass-to-charge values. In consequence, an imperfect mass calibration introduces imprecision in the fitted peak intensities, particularly for weaker signals in the presence of larger neighbours (Cubison and Jimenez, 2015), although imprecision in the fitted intensity is a significant source of error even for isolated peaks (Corbin et al., 2015). In practice, the precision of the mass calibration is limited principally by (i) the spectrometer resolving power, for wider calibrant peaks have a less well-defined centroid position, (ii) counting statistics for the calibrant ions, and, non-ideally, (iii) the influence of neighbouring ions on assessment of calibrant peak position. Since (i) is limited by the hardware, it may be considered an intrinsic limitation during data analysis. Whilst narrower peaks would improve the fitted peak positions, the measured peak width is of course fixed during analysis and thus plays no role in the parameters that a user may tune to optimise the mass calibration. However, (ii) and (iii) are worth consideration as they can significantly degrade calibration accuracy. We note that Corbin et al. (2015) demonstrate that the AMS calibration can also contain biases that are of similar magnitude as the imprecision; consideration of their sources is, however, outside the scope of this paper. Finally, it is emphasised that this discussion pertains to fitted peaks and these effects would not introduce appreciable error in integrated isobaric peak intensities (processing of the full-resolution mass spectra to centroid, or “stick”, spectra based on unit-mass resolution integration boundaries).

#### 3.2.1 Effect of counting statistics

A significant source of calibration imprecision during monitoring operation can be counting errors. In the lower mass range of the ToF-ACSM spectrum, several large signals arising from air and water ions (typically  $\text{H}_2\text{O}^+$ ,  $\text{N}_2^+$ ,  $\text{O}_2^+$  and  $\text{CO}_2^+$ ) may be used for mass calibration. Constraining the upper end is, however, significantly more challenging and

is typically achieved by including the tungsten ions in the calibrant peak list. As the ToF-ACSM is usually operated at half the emission current of the AMS (to maximise filament lifetime), these are weak signals and subject to a significant level of noise from counting error. Unfortunately, the inclusion of even one weak ion in the mass calibration peak list greatly increases calibration imprecision (Cubison and Jimenez, 2015). A similar simulation of the mass calibration routine used in that study was employed here to assess the impact of the weak  $\text{W}^+$  signal on the ToF-ACSM mass calibration imprecision. Comparison of the  $\text{N}_2^+$  and  $\text{W}^+$  ion signals for several ambient ToF-ACSM datasets indicates a ratio  $\text{N}_2^+/\text{W}^+ \sim 50\,000$ . Assuming a typical  $\text{N}_2^+$  signal of  $\sim 1 \times 10^5$  ions  $\text{s}^{-1}$ , we expect total ion counts over an integration period of a half hour (typical averaging time for mass calibration) of  $\sim 2 \times 10^8$  for  $\text{N}_2^+$  but only  $\sim 4 \times 10^3$  for  $\text{W}^+$ . The noise in the tungsten signal leads to relative calibration precisions of  $\sim 2$  ppm for  $m/\Delta m = 450$ . This value is, however, around an order of magnitude smaller than the biases in fitted position typically observed for the calibrant peaks (the difference in fitted peak position to that predicted from the calibration equation). It is nonetheless important that the spectra used for calibration are integrated over a sufficiently long period to ensure that imprecision arising from counting statistics is minimised. Thus, counting statistics do not contribute significantly to mass calibration error in the ToF-ACSM.

#### 3.2.2 Effect of isobaric ions

##### Identifying influence of isobaric ions

Use of the tungsten ions for mass calibration in the ToF-ACSM is further complicated by potential interference from poorly separated isobaric ions. Figure S5 compares ToF-ACSM data with higher-resolution data ( $m/\Delta m_{50} \sim 10\,000$ ) that clearly show the isobaric background organic ions (from EI ionisation of lab air) that contribute to the signal observed at the tungsten peaks. The limited mass resolving power of the ToF-ACSM leads to single broad peaks whose centroid values will be shifted to lower or higher  $m/Q$  according to the relative intensities of the various ions (Meija and Caruso, 2004).

However, it is still appropriate to utilise the tungsten peaks for mass calibration purposes when their signal is sufficiently large that the influence of the background peaks becomes negligible. Figure 3 compares lab data for clean and recently vented, i.e. dirty, vacuum chambers. In the absence of significant background, as may be expected for ambient data in remote locations after a few days of pump-down, the tungsten ion signals are 1–2 orders of magnitude larger than the neighbouring peaks. This decreases for a recently vented system to a factor of only 2–5 and with low filament emission currents can be expected to be even less. As the resolving power is not sufficient to unequivocally separate the tungsten ions from

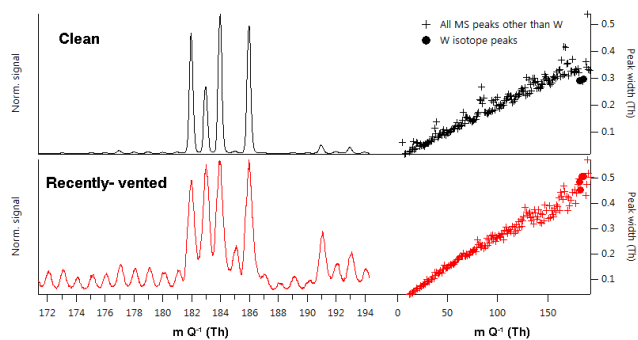


**Figure 3.** Left: example ToF-ACSM mass spectra for clean and recently vented (i.e. dirty) vacuum chambers, showing the tungsten isotope ion pattern superimposed on background peaks of different relative magnitudes. Right: width of the isobaric peaks as a function of mass to charge for the same MS. The solid circles denote the isobars containing the tungsten isotope peaks. These lie under the general trend in the clean case but follow the trend in the recently vented case. Owing to instrument tuning, the peaks are generally broader in the recently vented case.

the organic ions at the same nominal mass, this leads to peak broadening and a centroid position that does not accurately reflect that of the tungsten ions (see e.g. Meija and Caruso, 2004). Peak fits with freely varying positions and intensities were applied to each of the four isobaric MS peaks where the tungsten isotopes can be measured (182, 183, 184 and 186 Th). The offsets of the fitted positions to the true tungsten isotopes were respectively  $-0.9$ ,  $0.6$ ,  $0.0$  and  $-0.9$  ppm in the clean case and  $-28$ ,  $+152$ ,  $60$  and  $-95$  ppm in the recently vented case. For peaks with mass resolving powers of  $\sim 500$ , fitted positional imprecisions on the order of a few ppm are to be expected. The offsets observed in the clean case are thus expected and use of the tungsten isotopes for mass calibration of datasets from clean locations can be considered justified. However, for datasets with significant background the offsets are larger than would be realistic were the peaks to truly represent isolated ions; their use as calibrant peaks could introduce bias and/or imprecision in the mass calibration of magnitude  $\sim 100$  ppm. The ToF-ACSM analysis software contains an integrated tool for assessing the degree to which offsets in the fitted positions of calibrant ions affect the mass calibration. Users are strongly encouraged to use this tool in order to evaluate whether individual ions with isobaric interferences can be effectively used for mass calibrations.

An additional check on whether a peak represents an isolated ion or not is easily performed by considering the peak width as a function of  $m/Q$ , which should follow a straight-line relationship (Meija and Caruso, 2004). In the ToF-ACSM, the many interferences across the mass spectra lead to observed isobaric peak widths which usually broaden going to higher  $m/Q$ ; isolated ions at high  $m/Q$  stand out clearly as they lie under the trend, as is the case for tungsten

in the clean-chamber MS in Fig. 3. In contrast, for the recently vented-chamber MS the peak widths at 182, 184, 184 and 186 Th are broader than that which would be expected of isolated ions.

### Compensating for influences of isobaric ions

Meija and Caruso (2004) show that, when the peak width is larger than the mass difference of two neighbouring peaks, the expected centroidal peak in  $m/Q$  is approximately the weighted average of the isobar masses (their Eq. 8):

$$m_{\text{observed}} \sim x \times m_{\text{calibrant}} + (1 - x) \times m_{\text{influence}}, \quad (1)$$

where  $x$  is the relative abundance of the calibrant ion,  $m_{\text{calibrant}}$  the exact mass of the calibrant ion and  $m_{\text{influence}}$  the exact mass of an influencing peak. We propose that, in some cases, it may be justified to make a weighted adjustment of the mass positions of calibrant ions known to have influences from neighbouring, overlapping, peaks, based on the following assumptions:

- i. all influencing isobaric peaks can be grouped together and considered as one single influencing peak in Eq. (1);
- ii. the magnitude of the influencing peak is the same as the background peaks in the region of the MS where the calibrant ion is;
- iii. the exact mass of the influencing peak takes the same mass excess  $= m/Q - \text{mod}(m/Q)$  as the background peaks in the region of the MS where the calibrant ion is.

Clearly any adjustment to calibrant ion exact masses introduces a bias into the peak-fitting procedure and, as will be discussed later, an analysis of the sensitivity of the fitted peak intensities to the mass calibration should be performed, in which perturbations in the mass calibration are considered. However, the “best-case” scenario is when the mass calibration reflects the user’s best estimate of the true mass positions of the peaks; thus, if it is known that the calibrant ion peaks are shifted due to influencing, overlapping peaks, it may be argued that an attempt ought be made to correct for this, such that the sensitivity analysis starts from the best-estimated case. We note that we have chosen in this paper to use term mass excess rather than mass defect because, as in Kendrick’s original publication (Kendrick, 1963) describing the well-known “Kendrick plots”, mass defect is rather confusingly negative for masses with a positive offset from the nominal value.

We illustrate this methodology using the tungsten isotope ions as an example. A single peak (using the true mass spectral peak shape but allowing the width to vary) is fitted to each isobaric peak in the MS between 160 and 200 Th, encompassing the mass positions of the tungsten ions. The mean average peak intensity and mass excess of the surrounding peaks are calculated. Peaks of this intensity and

**Table 1.** Mass accuracy in ppm obtained using the true and compensated exact masses for the tungsten ions during mass calibration.

Ion	SF <sub>3</sub> <sup>+</sup>	SF <sub>4</sub> <sup>+</sup>	SF <sub>5</sub> <sup>+</sup>
Using true W <sup>+</sup> <i>m/Q</i>	-71	-21	-76
Compensated	-57	-3	-53

mass excess are used in Eq. 1 to calculate the corresponding position of the tungsten (calibrant) ions. Figure S6 exemplifies this approach. The surrounding isobaric peaks have an average mass excess of 0.095 Th and intensity of 665 ions (~ 15 times smaller than the tungsten peaks), leading to small positive shifts to the estimated “true” mass positions of the tungsten ions of ~ 0.006 Th (35 ppm).

In this example, the compensation for the influencing peaks would be applied in the mass calibration by entering not the true tungsten isotope exact masses (red circles in Fig. S6) but rather these values less the 35 ppm offset calculated above (yellow circles). To assess the validity of this method, the mass spectrum used in the example was recorded using a calibration gas SF<sub>6</sub> injected at the ioniser, giving rise to strong signals at the nominal masses 89, 108 and 127 Th from the ions SF<sub>3</sub><sup>+</sup>, SF<sub>4</sub><sup>+</sup> and SF<sub>5</sub><sup>+</sup> respectively. The mass calibration was performed based on the air peaks and the true or compensated tungsten peaks, and the mass offset of the SF<sub>3</sub><sup>+</sup>, SF<sub>4</sub><sup>+</sup> and SF<sub>5</sub><sup>+</sup> peaks calculated. As shown in Table 1, the mass accuracy was improved by ~ 20 ppm using the compensation technique described here.

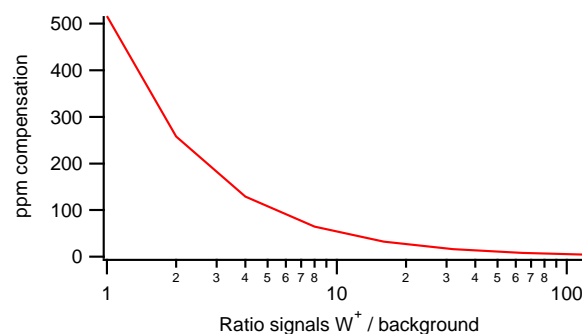
For the example MS used in these calculations, the tungsten ion peaks were ~ 15 times stronger than the surrounding peaks which we will refer to here as “background”, that is, the signal at the mass to charge ratios surrounding the calibrant ion signal. Assuming the same background peaks were present, but exhibited different intensities relative to the tungsten peaks, Fig. 4 shows the estimated relative compensation that would be applied. For a W<sup>+</sup>/background ratios of 100, a relative compensation of only 4 ppm is expected and this technique would have almost negligible effect on peak fitting at the mass resolving power of the ToF-ACSM. However, for a W<sup>+</sup>/background ratio of 5 (as may be expected in dirty environments), the relative compensation exceeds 100 ppm and use of the technique would need to be treated with the appropriate caution.

### 3.2.3 Alternative background peaks to tungsten ions

For datasets where the use of the tungsten ions in the mass calibration is not acceptable, an alternative constraint on the upper part of the MS is desired.

#### Trichloroethylene

We propose that the fragmentation pattern from the industrial solvent trichloroethylene is a potentially useful candidate for

**Figure 4.** Estimated relative compensation that would need to be applied to the W<sup>+</sup> exact mass owing to an influencing, overlapping, background peak separated by 0.095 Th and of relative signal strength indicated by the x axis.

ToF-ACSM (and AMS) mass calibration. Isotope patterns matching the NIST EI reference MS for trichloroethylene are apparent in multiple ToF-ACSM and AMS datasets. In particular, MS peaks which appear to correspond to the ions C<sub>2</sub><sup>35</sup>Cl<sub>3</sub>H<sup>+</sup> and C<sub>2</sub><sup>37</sup>Cl<sup>35</sup>Cl<sub>2</sub>H<sup>+</sup> at the nominal masses 130 and 132 Th, respectively, are often visible in ToF-ACSM mass spectra recorded in clean locations with low background. The time trend of the peak intensities for these ions follows that of the sensitivity of the instrument, indicating that the source of the interference lies within the vacuum chamber, most likely in the ionisation region. The peaks do not show up in the difference spectra and it is unlikely that trichloroethylene gas molecules from an external source could sufficiently penetrate the differential pumping system, which dilutes background gas molecule concentrations by a factor of 10<sup>7</sup>.

The identification of the isotope pattern at 130, 132 and 134 Th as trichloroethylene is supported by data from the HR-ToF-AMS. Figure 5 shows a HR-ToF-AMS MS recorded at the urban station in Helsinki (Mäkeläkatu) alongside a ToF-ACSM MS from the Neumayer station. Applying free-position peak fits as in Sect. 3.2.2 gave fitted peak positions deviating from those of the trichloroethylene ions of 0.2, -4.6 and 3.2 ppm in the HR-ToF-AMS (limited by counting statistics) and 0.9, 4.9 and 109 ppm in the ToF-ACSM MS for 130, 132 and 134 Th respectively. Whilst the trichloroethylene ions are clearly well separated from their neighbours by the HR-ToF-AMS, this is not the case for the ToF-ACSM and thus for calibration purposes the Trichloroethylene ion signals must, as was already pointed out for use of the tungsten ions, be significantly larger than the background in order to be considered as reliable mass calibration peaks. In the Neumayer dataset, the C<sub>2</sub><sup>35</sup>Cl<sub>3</sub>H<sup>+</sup> and C<sub>2</sub><sup>37</sup>Cl<sup>35</sup>Cl<sub>2</sub>H<sup>+</sup> signals were roughly 30 times larger than the background signal. The influence of the background ions is thus small and a relative centroid position shift of only 4 ppm is observed. A compensation of the exact masses during calibration as described above would thus have negligible effect. The same is not true for the weaker C<sub>2</sub><sup>37</sup>Cl<sub>2</sub><sup>35</sup>ClH<sup>+</sup> ion, whose centroid

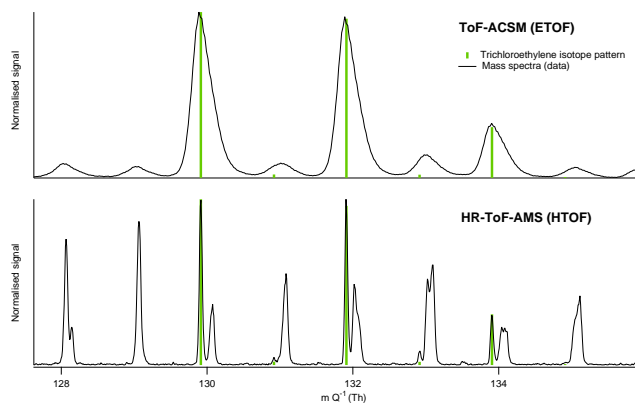


**Figure 5.** Mass spectra from the ToF-ACSM and HR-ToF-AMS showing the isotope pattern of trichloroethylene ( $C_2Cl_3H^+$ ).

position is shifted relative to the stronger isotope peaks by over 100 ppm.

For the Neumayer data, trichloroethylene proved to be a much more useful constraint on the upper region of the mass calibration than the tungsten ions, whose signal relative to background was an order of magnitude weaker. Nonetheless, it is important to note that the peaks do not represent truly isolated ions, as is clearly visible when comparing the HR-ToF-AMS and ToF-ACSM spectra in Fig. 5. Calibration biases of order a few ppm can be expected as a result and should be considered when assessing peak-fitting results, as will be discussed later.

### Extrapolation

In the absence of a valid constraint on the upper region of the mass calibration, the question is posed as to whether it is better to utilise the poorly defined calibrant peak regardless or simply extrapolate the calibration from the lower, well-defined, region of the MS. To investigate this, lab data were recorded where  $SF_6$  gas was injected directly into the ionisation region, leading to strong signals at unit masses 89, 108 and 127 Th from the ions  $SF_3^+$ ,  $SF_4^+$  and  $SF_5^+$  respectively. A mass calibration was performed using the square-root relationship  $ToF = a + b \times \sqrt{(m/Q)}$  and the calibrant peaks  $OH^+$ ,  $N_2^+$ ,  $O_2^+$ ,  $Ar^+$  and  $CO_2^+$ . The offsets from the true peak positions for  $SF_3^+$  and  $SF_4^+$  were then assessed for the extrapolated calibration and again when additionally using  $SF_5^+$  as a calibrant peak. For the constrained calibration (with  $SF_5^+$ ), offsets of  $-31$  and  $25$  ppm were found for  $SF_3^+$  and  $SF_4^+$  respectively. Without the  $SF_5^+$  constraint, these changed to  $-71$  and  $-19$  ppm respectively, a difference of up to approximately  $-40$  ppm. In Sect. 3.2.2 it was shown how interferences around the tungsten ions could lead to centroid peak position shifts of  $> 100$  ppm, indicating that an extrapolated calibration could indeed be preferred over introduction of a bias of unknown direction and magnitude due to interferences at the calibrant peaks.

It is noted that the offsets (biases) of a few tens of ppm represent the limiting average mass accuracy across the MS range that may be expected during routine ToF-ACSM operation. Careful calibrant selection, fitting of a sub-range and/or use of more complicated ToF/mass relationships may increase accuracy to below 10 ppm, but during normal operation the user should expect mass axis biases of around 10–20 and 50–100 ppm in the lower and upper regions of the MS respectively. Fitted peak intensities should be evaluated accordingly (see Corbin et al., 2015, for a detailed discussion on the influence of calibration bias on fitted peak intensity).

### Addition of calibrant compounds

In the HR-ToF-AMS, the use of a plastic servomotor inside the vacuum chamber leads to a background peak at 149 Th from the ionisation of the phthalate molecules leaching out from the plastic. This is a useful and commonly used calibrant peak that is, however, missing from the ToF-ACSM MS, as the instrument does not utilise this particular component. In the Q-ACSM, a naphthalene source is intentionally installed in the ioniser region to generate known background peaks for both transmission correction and mass calibration. In the interest of securing a decent calibration, installation in the vacuum chamber of a naphthalene source or a simple plastic element known to release phthalates into the environment could be a useful future modification to the instrument.

### 3.3 Peak-fitting uncertainties and terminology

Cubison and Jimenez (2015) give parameterisations to estimate the precision,  $\sigma_I$ , on fitted peak intensity for a system of two overlapping peaks using the same constrained peak-fitting procedure employed in this study. The two dependent parameters are the ratio of the two peak intensities,  $R_I$ , and the peak separation normalised to half-width at half-maximum (HWHM),  $X$ . As  $R_I$  increases, the precision with which the intensity of the less-intense ion peak can be fitted degrades. As  $X$  decreases, the same is true for both the more- and less-intense peaks. As a general rule, for  $R_I$  up to  $\sim 10$ , the fitted intensity of the child peak can be retrieved with acceptable precision for  $X$  as low as  $\sim 0.7$ . For smaller  $X$ , the imprecision increases and obtaining reliable results becomes challenging and eventually impossible. Peaks separated by  $X > 1.6$  can nearly always be reliably fitted, except in the case of  $R_I > 200$ , above which the imprecision on the fitted parameters of the less-intense peak is so great as to preclude their use in data analysis. It is noted that Cubison and Jimenez (2015) assumed a constant peak shape in deriving this parameterisation, which thus represents the best-case scenario and should be interpreted accordingly. We make use of this parameterisation in this study when discussing peak separations, which we state henceforth as  $X$ , i.e. normalised to HWHM.

## 4 Results and discussion

### 4.1 Ammonium

Data collected at the urban background station, SMEAR III, are used to study fitting of main inorganic ions, ammonium, nitrate and sulfate. Peak fitting is routinely used on HR-ToF-AMS spectra to determine ammonium signal intensities, as  $\text{NH}_2^+$ ,  $\text{NH}_3^+$  and  $\text{NH}_4^+$  all have large isobaric interferences (from  $\text{O}^+$ ,  $\text{HO}^+$  and  $\text{H}_2\text{O}^+$  respectively) and the integrated data time series, constructed based on molecular fragmentation patterns which account for these large interferences (Allan et al., 2004), are thus noisy and detection limits correspondingly high. Fröhlich et al. (2013) applied peak fitting to ToF-ACSM spectra and concluded that the  $\text{NH}_x$  ions were unresolvable from the interfering ions; we extend this discussion, with reference to the peak separations and expected intensity ratios, as the  $\text{NH}_x$  ions exemplify how the intensities of well-separated peaks cannot always be accurately fitted. In the case of  $\text{NH}_2^+$ ,  $\text{NH}_3^+$  and  $\text{NH}_4^+$ ,  $X$  approaches unity and the peaks can be considered partially separated. However, for peak ratios over 100 as are observed for these ions,  $X > 1$  is required even to achieve precisions on fitted intensity,  $\sigma_I$ , of 100 % (Cubison and Jimenez, 2015), effectively precluding successful peak fitting for all but the strongest ammonium signals. The only possibility for extracting useful information on ammonium from peak fitting is thus at 15 Th where the interferences on  $\text{NH}^+$  are much smaller, as exemplified in Fig. 6. However, with peak separations to the neighbouring ions of  $X = 0.5$ , the imprecision expected in the fits is still large. Batch peak fitting at 15 Th on ammonium nitrate calibration data yielded a time series for  $\text{NH}^+$  whose signal : noise was similar to that of the integrated peak time series. However, peak fitting did not improve the quality of the data and thus for ammonium could only be used to help support assumptions required to construct the integrated data fragmentation table. It is estimated that mass resolving power approaching 1000 in this lower region of the MS would be required in order to reliably deconvolve the ammonium peak intensities.

### 4.2 Nitrate

In AMS analysis, concentrations of aerosol species from integrated unit-mass data are calculated based on well-described fragmentation patterns (Allan et al., 2004). Previous studies have shown that, in many ambient conditions, the default fragmentation patterns work well. However, in the case of high organic loadings and particularly during biomass-burning events, the assumptions tend to break down and nonsensical mass concentrations may result (e.g. Ortega et al., 2013). In general, it is preferred to construct the time series from the sum of individual fitted ion intensities, providing of course that the uncertainty on these values is not large.

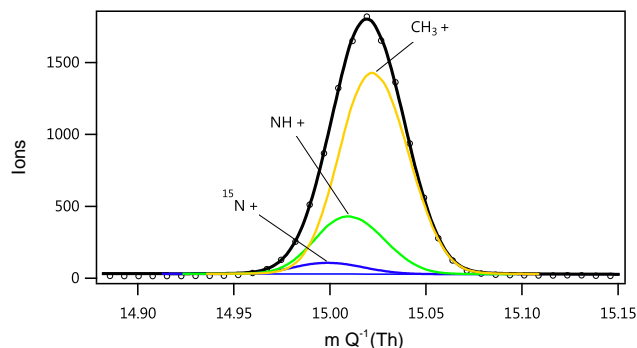


**Figure 6.** The isobaric peaks  $^{15}\text{N}^+$  ( $m/Q = 14.9996$  Th),  $\text{NH}^+$  ( $m/Q = 15.01035$  Th) and  $\text{CH}_3^+$  ( $m/Q = 15.0229$  Th) at 15 Th have peak separations of 0.5 half-widths for mass resolving power  $m/\Delta m = 300$ .

Inorganic nitrate is an important aerosol component whose principal contributing ion signals,  $\text{NO}^+$  and  $\text{NO}_2^+$ , both suffer from isobaric interferences due to neighbouring organic ions. Although Fröhlich et al. (2013) reported that it should be possible to use peak fitting to resolve these interferences, the peak separations are very small indeed and no uncertainties or confidence metrics were presented. We address these issues here in detail.

At 30 Th the peak separations of  $\text{NO}^+$  from the organic isobaric interferences  $\text{CH}_2\text{O}^+$  and  $\text{C}_2\text{H}_6^+$  are  $X \sim 0.3$  and 1.3 respectively (Fig. 7). A similar situation presents itself for  $\text{NO}_2^+$  at 46 Th (isobaric ions  $\text{CH}_2\text{O}_2^+$  and  $\text{C}_2\text{H}_6\text{O}^+$ ). Calculating peak intensity via peak fitting on fixed-position peaks separated by  $X \sim 0.3$  is extremely sensitive to the mass calibration. However, fortuitously in this case, the isobars 30 and 46 Th both lie close to calibrant ions used in the mass calibration; in the case of 30 Th the isobar is surrounded by  $\text{N}_2^+$  at 28 and  $\text{O}_2^+$  at 32 Th. As a result, the bias expected in the calibration is very small relative to other regions in the mass spectrum (where the calibration may be extrapolated) and its magnitude can be predicted from the biases of the calibrant ions themselves.

Given the expected sensitivity of the highly overlapping fits to the mass calibration, it is appropriate to conduct a sensitivity analysis to assess the degree of confidence that might be drawn from the fitted intensity values. Tofware offers a graphical tool for this purpose. An example is given for the isobar 30 Th, with fitted ions  $\text{NO}^+$ ,  $\text{CH}_2\text{O}^+$  and  $\text{C}_2\text{H}_6^+$ , in Fig. 8, using data from the SMEAR III campaign. Using the ions  $\text{H}_2\text{O}^+$ ,  $\text{N}_2^+$ ,  $\text{O}_2^+$  and  $\text{CO}_2^+$  to perform the mass calibration gave mass accuracies of between 2 and 13 ppm. Assessment of the sensitivity of the fitted intensities at 30 Th to mass calibration bias does not therefore need to consider much larger values than this; we conservatively chose 20 ppm, which equates to about 5 % of the separation of the ions  $\text{NO}^+$  and  $\text{CH}_2\text{O}^+$ . In the general case, a larger perturba-

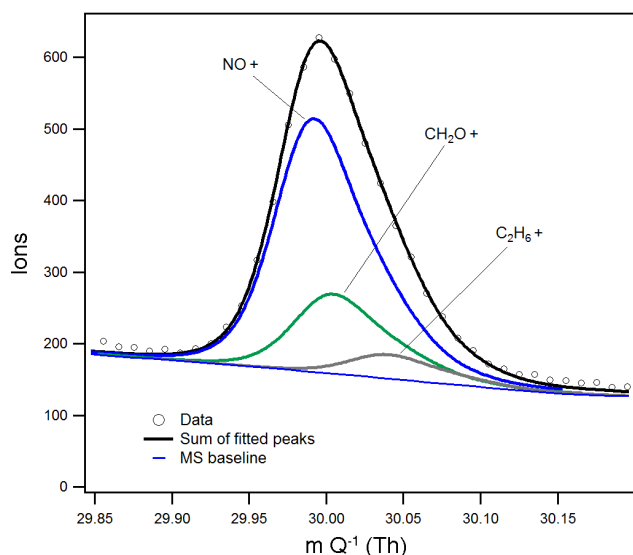


**Figure 7.** The isobaric peaks from  $\text{NO}^+$  ( $m/Q = 29.997$  Th) and  $\text{CH}_2\text{O}^+$  ( $m/Q = 30.010$  Th) at 30 Th have a peak separation of 0.34 half-widths for resolving power  $m/\Delta m = 400$ .

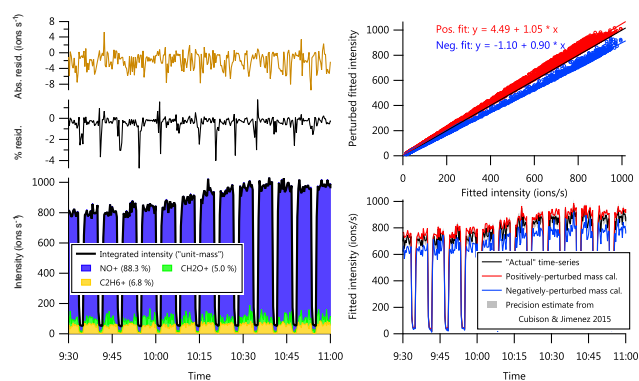


**Figure 8.** Assessing the sensitivity of the fitted peak intensity of the  $\text{NO}^+$  ion as a function of time to perturbations in the mass calibration of  $\pm 20$  ppm. Left: the sum of the ions fitted at this peak compared with the integrated signal (bottom) and the absolute and relative residuals (top). Top right: scatter plots of the fitted  $\text{NO}^+$  signals for the perturbed vs. best-case mass calibration scenarios. Bottom right: time series of the fitted  $\text{NO}^+$  intensities, with the perturbed mass calibration cases shown in red and blue. The shading around the black line indicates the expected precision predicted by the parameterisation of Cubison and Jimenez (2015).

tion value of between 50 and 100 ppm would be appropriate, depending on the confidence in the calibration.

From Fig. 8 one can take confidence that the fitted  $\text{NO}^+$  ion intensities are reliable. Firstly, consider the time series of the fitted vs. integrated peak intensities and their residuals for the unperturbed mass calibration (left panels). The sum of the fitted peak intensities matches the integrated values to within a few percent (Figs. 8 and S7). For 20 s averaging of a peak with a significant non-zero MS baseline and closely

separated neighbouring isobaric peaks (which influence the integrated intensities), this level of agreement is indeed indicative that the peak-fitting process has been properly performed. The step changes in the summed fitted intensity as the aerosol filter is switched in/out of the inlet line are also accurately captured.

The influence of perturbing the mass calibration is shown in the right panels as a time series (bottom) and scatter plot (top). When positively perturbing the calibration by 20 ppm (shifting the entire mass axis  $20 \text{ ppm} = 30 \text{ Th} \times 20/1 \times 10^6 = 0.0006 \text{ Th}$  but holding peak positions fixed), the fitted  $\text{NO}^+$  intensity increases by 10 %. A negative perturbation of similar magnitude would decrease fitted intensity by 12 %. It is important to note that this is a sensitivity analysis and not an uncertainty calculation on the fitted intensities; nonetheless the method does offer a useful validity check on the fitted parameters. We henceforth refer to the relative intensity bias (offset, in percent) introduced by calibration perturbation as  $\Delta I$ .

Regarding the perturbed time series, the estimated precision on fitted intensity from the parameterisation of Cubison and Jimenez (2015),  $\sigma_I$ , is also shown on the unperturbed intensity time series (shaded area, bottom right panel). The fitted intensity of the  $\text{NO}^+$  ion is deconvolved with  $\sigma_I$  less than a few percent. Although this example presents a truly challenging peak-fitting scenario with limited signal and a large degree of peak overlap, one may draw conclusions based on the actual fitted peak intensities provided they held true for changes of roughly  $\pm 10$  %. Similar conclusions may also be drawn looking at  $\text{NO}_2^+$  at 46 Th (Fig. S8).

It is noted that this assessment of the uncertainties assumes an invariant and correctly defined peak shape. Inaccuracies in the peak shape arising from either instrumental artefacts or user error in its definition would propagate into errors in the fitted intensities discussed above. Although a quantitative assessment of these effects is outside of the scope of this study, we illustrate the impact of an incorrect peak shape by comparing the fit results for  $\text{NO}^+$  and its interferences using the user-defined and Gaussian peak shapes. For a representative MS from the SMEAR dataset, we observe that 73 % of the area is assigned to the  $\text{NO}^+$  ion using peak fitting with the user-defined shape. Using Gaussians, this increases to 87 %, a relative change of +19 %. Whilst such a large inaccuracy in peak shape would not be expected (and indeed the fit residuals are large and apparent using Gaussians), this highlights the importance of carefully defining the peak shape as described in Sect. 3.1.2.

Finally, it is noted that, for the data shown, the organic mass loading was approx. 1.5 times that of the nitrate. In spectra with large organic signals, the relative strength of the nitrate ions to the organic interferences would be smaller and the corresponding uncertainty larger. Nonetheless, the same methodology presented here could be applied to assess the uncertainties.

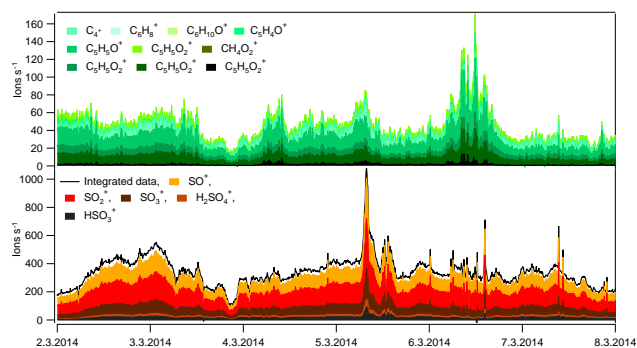


**Figure 9.** Concentrations of main sulfate ions ( $\text{SO}^+$ ,  $\text{SO}_2^+$ ,  $\text{SO}_3^+$ ,  $\text{HSO}_3^+$  and  $\text{H}_2\text{SO}_4^+$ ) from peak fitting and sulfate calculated from application of the fragmentation table with integrated data (lower panel) and time series of the isobaric organic ions in the same  $m/Q$  as sulfate fragments (upper panel).

### 4.3 Sulfate

Sulfate is a further important inorganic aerosol component measured by the ToF-ACSM. The principal contributing ions,  $\text{SO}^+$ ,  $\text{SO}_2^+$ ,  $\text{SO}_3^+$ ,  $\text{HSO}_3^+$  and  $\text{H}_2\text{SO}_4^+$ , are all affected by isobaric organic influences and the total sulfate concentration from integrated peak data over the nominal masses is, as per ammonium and nitrate, calculated based on assumed fragmentation patterns to account for these influences (henceforth referred to simply as “integrated data”). Like nitrate, these assumptions tend to break down for high organic mass loading and particularly for biomass burning. However, with  $X$  values relative to the closest organic interferences of 0.5–0.8, constrained peak fitting can be employed to directly calculate the sulfate ion signals with acceptable uncertainty. To demonstrate this, peak fitting was performed on the SMEAR III dataset and an analogous sensitivity analysis was performed as presented for nitrate in the previous section (Figs. S9–S13). The mass calibration perturbation employed for these sensitivity analyses reflected the position of the ions under study in the mass spectrum, relative to those used to perform the calibration ( $\text{H}_2\text{O}^+$ ,  $\text{N}_2^+$ ,  $\text{O}_2^+$  and  $\text{CO}_2^+$ ). Thus, the confidence in the mass calibration at 48 Th ( $\text{SO}^+$ ) is quite high and a 20 ppm perturbation was applied. In contrast at 98 Th ( $\text{H}_2\text{SO}_4^+$ ), the calibration is somewhat extrapolated and a 50 ppm perturbation was applied. An example of perturbed time series for  $\text{SO}^+$  ion is in Fig. S14. The resulting sensitivities of the fitted intensities to calibration perturbations,  $\Delta_I$ , ranged from approx. 3 to 30 %.

The SMEAR III data are used to demonstrate construction of a mass-loading time series for sulfate based on the sum of the sulfate ion signals retrieved from peak fitting (Fig. 9). The sum of the fitted intensities was able to reconstruct the same time series as that from the fragmentation table with only 3 % difference (integrated  $\sim 1.03 \times$  fitted), demonstrating the validity of the method. Figure 9 shows the fitted intensities of

the isobaric interferences from organic ions. The ratio of the organic signal from the integrated data to the sum of the fitted intensities of the organic ions is  $0.64 \pm 0.40$ . Overall, the peak-fitting method weighted the allocation of the ion signals more heavily towards organic than the fragmentation table approach. However, the differences are small and the only significant conclusion that may be drawn is that, for this dataset, the methods are consistent for a sulfate to within a few percent.

### 4.4 Sodium chloride

The Neumayer station, situated in a clean environment adjacent to the open ocean, provides an ideal location to study compounds originating from the sea. Data collected on Neumayer station were used to study peak fitting of sodium, chloride and methanesulfonic acid. The mass calibration for the Neumayer dataset was performed using the following calibrant ions;  $\text{H}_2\text{O}^+$ ,  $\text{N}_2^+$ ,  $\text{O}_2^+$ ,  $\text{Ar}^+$ ,  $\text{CO}_2^+$ ,  $\text{SO}_2^+$ ,  $\text{C}_2^{35}\text{Cl}_3\text{H}^+$  and  $\text{C}_2^{35}\text{Cl}_2^{37}\text{ClH}^+$ . The isolated ion peak shape was used rather than a Gaussian to optimise the calibrant ion fits. Mass accuracy was in the range 10–20 ppm for all calibrant ions.

On 2 and 3 December 2014, elevated aerosol chloride was observed at the Neumayer station (Figs. S15–S16). Air-mass back trajectories (Global Data Assimilation System (GDAS) data, NOAA Hybrid Single-Particle Lagrangian Integrated Trajectory model (HYSPPLIT, v4.9); Draxler and Rolph, 2013) show that the air mass was transported along the Antarctic coastline at low altitudes during the previous days, pointing to the influence of sea salt as an explanation for the observed chloride concentrations of up to  $300 \text{ ng m}^{-3}$  (Fig. S15). Neither MSA, proxied by  $m/Q$  79, nor organic aerosol was elevated during this period. Peak fitting was conducted on the mass spectra from this episode to (i) demonstrate the presence of sea-salt-related compounds and (ii) generate a time series for  $\text{NaCl}^+$ , separated from its isobaric organic interference(s). The chloride ions  $^{35}\text{Cl}^+$  and  $^{37}\text{Cl}^+$  have only relatively tiny interferences in ToF-ACSM mass spectra and thus no meaningful additional information can be expected to be gained from peak fitting relative to the integrated peak data, except perhaps in exceptionally large organic plume cases.

Several ions attributable to sea salt (following Schmale et al., 2013.), such as  $\text{Na}^{35}\text{Cl}^+$  (57.958 Th),  $\text{Na}^{37}\text{Cl}^+$  (59.956 Th),  $\text{Fe}^{35}\text{Cl}_2^+$  (125.87 Th) and  $\text{Fe}^{37}\text{Cl}^{35}\text{Cl}^+$  (127.87 Th), could be identified in the average mass spectrum from this period, as shown in Fig. 10. In the case of  $\text{NaCl}^+$ , three interfering isobaric organic ions are known to be visible in ToF-ACSM mass spectra; at this mass resolving power it is not possible to state which of these are observed here, although the oxygenated peak  $\text{C}_3\text{H}_6\text{O}^+$  is a likely candidate and is demonstrated in Fig. 10. However, irrespective of the interference(s) chosen, sensitivity of the fitted intensity of  $\text{NaCl}^+$  to a 100 ppm mass calibration perturbation was  $\sim 5$  %, indicating that the majority of the

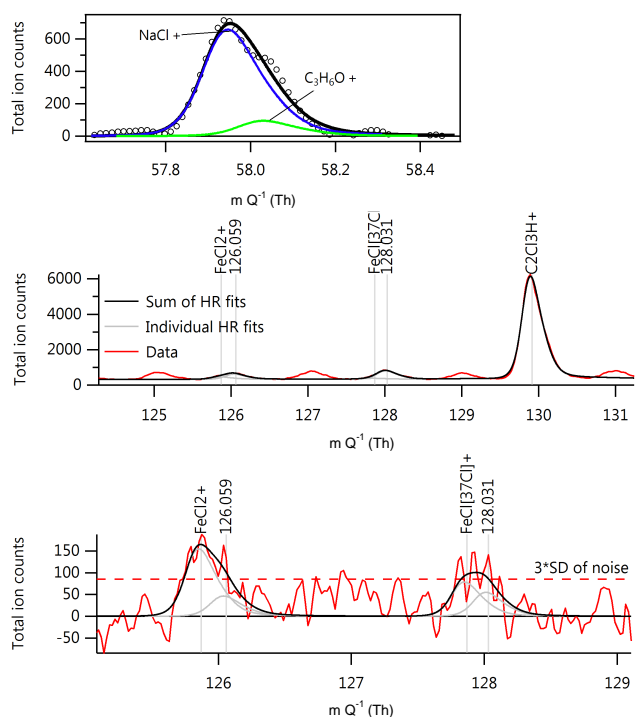


**Figure 10.** Top: Isobaric peaks of  $\text{NaCl}^+$  and  $\text{C}_3\text{H}_6\text{O}^+$ . Centre: total mass spectrum showing the calibrant ion  $\text{C}_2\text{Cl}_3\text{H}^+$  and signals from unknown compounds at nominal masses 126 and 128 Th. Bottom: difference mass spectrum (ambient minus filter) showing statistically relevant signals from the isotopes  $\text{Fe}^{35}\text{Cl}_2^+$  and  $\text{Fe}^{37}\text{Cl}^{35}\text{Cl}^+$ .

difference signal at 58 Th could indeed be attributed to this ion.

The  $\text{FeCl}^+$  ions are shown as a further example of sea salt compounds that could be unambiguously identified in the Neumayer data. The centre panel in Fig. 10 shows a portion of the average total mass spectrum together with peak-fitting curves for the period during which elevated chloride was observed. The mass calibrant ion  $\text{C}_2\text{Cl}_3\text{H}^+$  at 130 Th is visible in addition to unknown background ion(s) at 126 and 128 Th. For the difference mass spectrum, however, these background ions contribute only to the noise and two aerosol signals are resolvable above the noise level, defined as 3 times the standard deviation over the adjacent mass range. These signals are well represented by the  $\text{Fe}^{35}\text{Cl}_2^+$  and  $\text{Fe}^{37}\text{Cl}^{35}\text{Cl}^+$  isotopes; the mass excess of these aerosol peaks is significantly ( $\sim 1500$  ppm) less than the background peaks observed for the total mass spectrum. We note that it is almost certain that the signal from a multitude of unresolvable organic ions combines together to give the apparent single background peak, but in this analysis we are only concerned with the relatively well-separated sea salt signals. Further support to their identification is given by the ratio of the signal intensities.  $^{37}\text{Cl}$  exhibits only 32 % the abundance of the  $^{35}\text{Cl}$  isotope, and thus an intensity ratio of 67 % is ex-

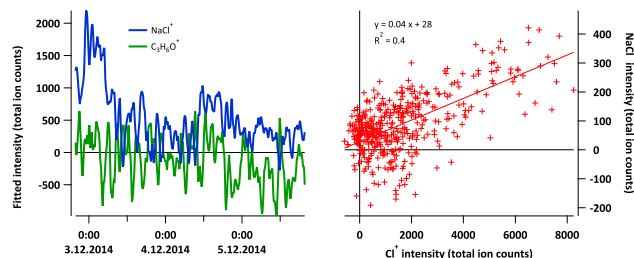


**Figure 11.** Left: time series (1 h integration period) of the fitted intensities for the isobaric ions  $\text{NaCl}^+$  ( $m/Q = 57.96$  Th) and  $\text{C}_3\text{H}_6\text{O}^+$  ( $m/Q = 58.04$  Th). Right: correlation of the  $\text{NaCl}^+$  ion signal with that of  $\text{Cl}^+$  (10 min integration period).

pected between these peaks, in acceptable agreement with the observed 59 % from the fitted peak intensities given the weak signal levels.

The time series of fitted peak intensities also supports the hypothesis that the aerosol chloride can be attributed to sea salt, for the trends of  $\text{Cl}^+$  and  $\text{NaCl}^+$  are moderately correlated ( $R^2 = 0.4$ ), as shown in Fig. 11. The signal intensities of  $\text{NaCl}^+$  are weak and the noise in the organic background signal at 58 Th from  $\text{C}_3\text{H}_6\text{O}^+$  is significant, but it shows no apparent correlation with the chloride signal.

Ovadnevaite et al. (2012) demonstrated using laboratory testing and ambient data that sea salt can be quantitatively measured with HR-ToF-AMS. They demonstrated that altogether 36 high-resolution ions contributed to the sea salt fragmentation pattern, but only 7 ions had a significant influence on the derived aerosol mass, namely  $^{23}\text{Na}^+$ ,  $^{35}\text{Cl}^+$ ,  $\text{H}^{35}\text{Cl}^+$  and  $^{23}\text{Na}^{35}\text{Cl}^+$  and their isotopes  $^{37}\text{Cl}^+$ ,  $\text{H}^{37}\text{Cl}^+$  and  $^{23}\text{Na}^{37}\text{Cl}^+$ . In clean Antarctic conditions with minimum interference from organic ions ToF-ACSM can detect  $^{23}\text{Na}^+$ ,  $^{35}\text{Cl}^+$ ,  $\text{H}^{35}\text{Cl}^+$  and  $^{23}\text{Na}^{35}\text{Cl}^+$  ions and their isotopes.

#### 4.5 Methanesulfonic acid

Oceans release dimethyl sulfide, which is further oxidised to several sulfur compounds, such as  $\text{SO}_2$ ,  $\text{H}_2\text{SO}_4$  and MSA (Gondwe et al., 2003; Yin et al., 1990). Previous studies have demonstrated that the AMS can be used to measure MSA concentrations of submicron particles (Phinney et al., 2006; Schmale et al., 2013).

From 7 to 13 January 2015, elevated sulfate (up to  $2 \mu\text{g m}^{-3}$ ) and MSA concentrations were observed at the Neumayer station (Fig. S17). At Neumayer, the interference from isobaric ions was very low (Fig. S18). All typical MSA fragments (Schmale et al., 2013; Phinney et al., 2006) were relatively strong signals relative to their isobaric interferences and could be straightforwardly identified in the mass spectra:  $\text{CH}_3\text{S}^+$  (44.98 Th),  $\text{CH}_3\text{S}^+$  (47.00 Th),  $\text{HSO}_2^+$  (64.97 Th),  $\text{CH}_2\text{SO}_2^+$  (77.98 Th),  $\text{CH}_3\text{SO}_2^+$  (78.99 Th) and  $\text{CH}_4\text{SO}_3^+$  (95.99 Th) (Fig. 12, Table 2). A good correlation between the main ions ( $\text{HSO}_2^+$ ,  $\text{CH}_3\text{SO}_2^+$  and  $\text{CH}_4\text{SO}_3^+$ ) with

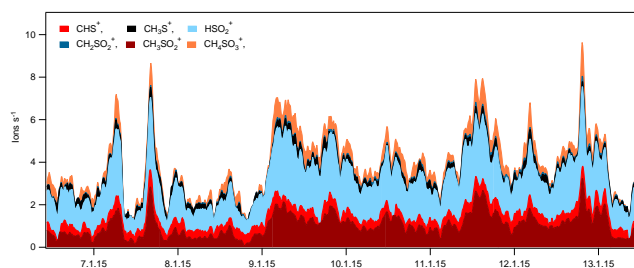


**Figure 12.** Time series of MSA fragments  $\text{CHS}^+$  (44.98 Th),  $\text{CH}_3\text{S}^+$  (47.00 Th),  $\text{HSO}_2^+$  (64.97 Th),  $\text{CH}_2\text{SO}_2^+$  (77.98 Th),  $\text{CH}_3\text{SO}_2^+$  (78.99 Th) and  $\text{CH}_4\text{SO}_3^+$  (95.99 Th) during episode 2.

**Table 2.** Observed MSA ions, their principal isobaric ions and peak separation

Ion	$m/Q$ (Th)	Principal isobaric ions	Peak separation $X$
$\text{CHS}^+$	44.979347	$\text{C}_2\text{H}_5\text{O}^+$ , $^{13}\text{CO}_2$	0.2
$\text{CH}_3\text{S}^+$	46.994999	$\text{CH}_3\text{O}_2^+$ , $\text{CCl}^+$	0.3
$\text{HSO}_2^+$	64.969177	$\text{C}_4\text{HO}^+$ , $\text{C}_5\text{H}_5^+$	0.4
$\text{CH}_2\text{SO}_2^+$	77.977005	$\text{C}_5\text{H}_2\text{O}^+$ , $\text{C}_6\text{H}_6^+$	0.3
$\text{CH}_3\text{SO}_2^+$	78.984825	$\text{C}_5\text{H}_3\text{O}^+$ , $\text{C}_6\text{H}_7^+$	0.3
$\text{CH}_4\text{SO}_3^+$	95.987564	$\text{SO}_4^+$	0.2

highest signals was observed (Fig. S19, Table S1). However, we note that for all MSA ions the separation from isobaric ions was low ( $X = 0.2\text{--}0.4$ ), thus increasing the uncertainty of the results. In typical conditions with larger background and/or organic signals, this analysis would become difficult and uncertainties large. In clean conditions ToF-ACSM provided the possibility to discern between and measure both sulfate and MSA fragments, which combined with meteorological data could be used to e.g. further study the CLAW hypothesis (Charlson et al., 1987).

#### 4.6 Metals

Data collected in an underground mine are used to study the peak fitting of ions from semi-volatile metals. It has been demonstrated that the ToF-AMS, upon whose technology the ACSM is based, is capable of detecting ions associated with the metals Cu, Zn, As, Se, Sn and Sb (Salcedo et al., 2012). Further semi-volatile elements may also be measurable based on their melting or thermal decomposition points (Drewnick et al., 2015). In the mine environment it is expected that metallic elements comprise a significant fraction of the aerosol mass (Csavina et al., 2012). The underground mine dataset is thus a good example of a first assessment of the capability of the ToF-ACSM to detect metal species. The ions of these species tend to have large mass excesses and are often separated from their neighbouring ions by  $X > 1$ , indicating that peak fitting should be able to resolve their signals.

**Table 3.** Peak separation  $X$ , normalised to HWHM, of various metals ions from neighbouring ions for instrumental mass resolving power of  $m/\Delta m = 450$ .

Element	Ion	Peak separation $X$ from closest neighbouring ion (normalised to HWHM)
As	$^{75}\text{As}^+$ , $^{75}\text{As}_2^+$	1.0
Cu	$^{63}\text{Cu}^+$	1.0
	$^{65}\text{Cu}^+$	1.2
Sb	$^{121}\text{Sb}^+$	1.2
	$^{123}\text{Sb}^+$	1.0
Se	$^{74}\text{Se}^+$	1.2
	$^{76}\text{Se}^+$ , $^{77}\text{Se}^+$	0.9
	$^{78}\text{Se}^+$	1.1
	$^{80}\text{Se}^+$	0.1
Sn	$^{116}\text{Sn}^+$ , $^{118}\text{Sn}^+$	1.1
	$^{120}\text{Sn}^+$	1.5
Zn	$^{64}\text{Zn}^+$	0.4
	$^{66}\text{Zn}^+$ , $^{67}\text{Zn}^+$ , $^{68}\text{Zn}^+$	1.2
	$^{70}\text{Zn}^+$	1.5

These peak separations are given in Table 3 for the isotopes of the metals reported detectable by Salcedo et al. (2012).

High signal levels, such as those observed in the mine (up to  $200 \mu\text{g m}^{-3}$ ), clearly improve peak fitting, as the description of the peak shape is well defined by the discrete data points with high signal : noise ratio. However, the multiple interferences at nearly every isobar precludes a truly accurate mass calibration and certain assumptions must be made when performing this analysis step. Consequently, a careful sensitivity analysis must be performed before drawing conclusions from the fitted peak intensities. To highlight the performance of the instrument and fitting procedure in measuring changes in mass component intensities, a period at the end of a working day was chosen for detailed analysis, when the organic mass loading in the mine falls sharply from  $> 30$  to  $< 3 \mu\text{g m}^{-3}$  over a 2 h period.

As many of the metals isotopes exhibit mass excesses that differ significantly from other (in most cases organic) peaks in the MS, representation of the fitted position in  $m/Q$  of each isobaric peak in a mass excess plot can be used to highlight features of interest, as shown in Fig. 13. Certain peaks stand out from the general pattern as having mass excesses that deviate from the general trend, principally those from  $\text{SO}_x$  (48, 64, 66) and  $\text{As}_x$  (75, 150). It is noted that there is a contribution from  $^{66}\text{Zn}^+$  at 66 Th which also contributes to the observed negative mass excess. A more detailed investigation was thus undertaken to assess potential signals from the As and Zn ions.

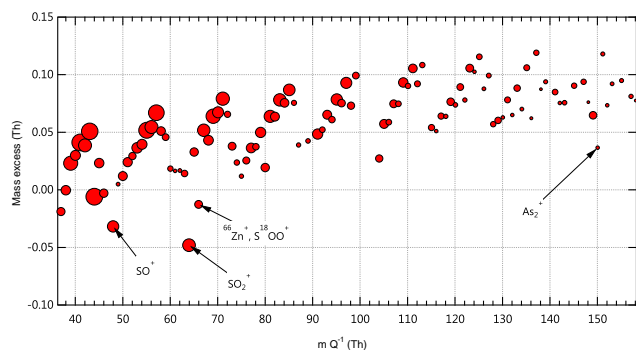


**Figure 13.** Mass excess plot for the isobaric peaks visible in a MS from the underground mine data. The peaks containing the Arsenic and  $\text{SO}_x$  ions are indicated. The data points are sized according to the log of the peak intensity.

#### 4.6.1 Mass calibration

The high mass loadings encountered during the mine study led to a large instrument background, which remained elevated overnight. The tungsten isotope pattern was occluded and these ions could not be used in the mass calibration. However, the pattern of the trichloroethylene isotopes was evident during cleaner periods, albeit not without interference from overlapping organic background peaks. An example MS is shown in Fig. S20; the peaks at the isobars 130 and 132 Th, where the principal ions of trichloroethylene exists, are approximately 3 times as large as many of the surrounding organic background peaks. As no other identified isolated ions were available at masses greater than 44 Th ( $\text{CO}_2^+$ ), an attempt was made to constrain the high end of the mass calibration by employing the mass-compensation technique described in Sect. 3.2.2. As a result, the exact mass of the trichloroethylene ions in the mass calibration was increased by 0.04 Th or  $\sim 300$  ppm (the corresponding mass excess plot is given in Fig. S21). These ions, together with  $\text{N}_2^+$ ,  $\text{O}_2^+$  and  $\text{CO}_2^+$ , were used to apply a mass calibration for the entire time period of study. The compensation technique could not have been utilised for mass spectra during the working hours of the mine as the organic mass loading was too high (and the trichloroethylene peaks thus obscured to the extent that the calibration compensation technique would introduce unacceptably large errors into the fitted parameters). It is noted that, relative to the mass axis derived using this calibration technique, calibrating on the air peaks alone would have led to a mass offset of  $-57$  ppm at 150 Th (i.e. extrapolating to the high end of the MS). A sensitivity analysis must therefore account for mass calibration perturbations at least as large as this, preferably greater.

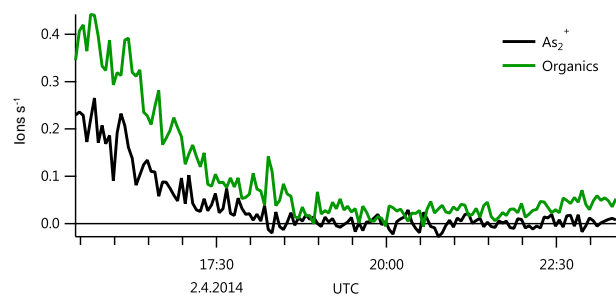


**Figure 14.** Time series of the mass loadings calculated from peak fitting for the isobaric peaks at 150 Th. The organics trace represents the sum of the signals from the peaks  $\text{C}_4\text{H}_6\text{O}_6^+$  and  $\text{C}_{10}\text{H}_{14}\text{O}^+$ .

#### 4.6.2 Time series of metal ions

After application of the mass calibration and determination of the peak width and shape using the methods described in Sect. 3.1, peak fitting was performed on the mine data with a peak list specifically chosen to assess the potential of the ToF-ACSM to deconvolve the metal ion signals from the interfering organic peaks. An example of the aerosol signal derived from the fitted peak intensities is shown in Fig. 14 for the arsenic ion  $\text{As}_2^+$  (an example mass spectrum from this time series showing the peak fits is shown in Fig. S22). Three ions have been fitted at 150  $m/Q$ :  $\text{As}_2^+$ ,  $\text{C}_4\text{H}_6\text{O}_6^+$  and  $\text{C}_{10}\text{H}_{14}\text{O}^+$ . The two organic ions are closely spaced ( $X < 0.4$ ) and we emphasise that we do not attempt to conclude whether the organic signal at 150 Th is attributable to either  $\text{C}_4\text{H}_6\text{O}_6^+$  or  $\text{C}_{10}\text{H}_{14}\text{O}^+$  (or otherwise) but seek only to separate the metal and organic signals as a whole. Although it was demonstrated for nitrate that highly overlapping peaks with similar  $X$  values could be deconvolved, the uncertainty in the mass calibration is much larger in this example, precluding the reliable separation of the organic signals. However,  $\text{As}_2^+$  and its assumed closest neighbour  $\text{C}_4\text{H}_6\text{O}_6^+$  are separated by  $X \sim 1.0$  and thus should be resolvable according to the results of Cubison and Jimenez (2015). As Fig. 14 shows, this does indeed appear to be the case. Both the organic and metal signals decrease in intensity at the end of the working day, but the organic remains at a measurable non-zero value overnight whereas the  $\text{As}_2^+$  decreases below the detection limit. A similar trend was apparent for the  $\text{As}^+$  ion (scatter plot in Fig. S23). It is noted that no attempt is made here to derive the true mass loadings of the metal and organic components, whose calculation is outside the scope of this peak-fitting paper and would require application of relative ionisation efficiencies which are still poorly understood (Salcedo et al., 2012). Finally, it is observed that use of the “Fast-MS” sampling technique described by Kimmel et al. (2011) allows time-resolved detection of slowly evaporating components in the difference data (ambient minus filter).

### 4.6.3 Sensitivity analysis

Given the assumptions made in applying the mass calibration, assessment of the sensitivity of the fitted peak intensities to calibration perturbations, analogously as was described in Sect. 4.2 for nitrate, was particularly important for this dataset. Figure S24 shows the results of this sensitivity analysis at 150 Th, with fitted ions  $\text{As}_2^+$ ,  $\text{C}_4\text{H}_6\text{O}_6^+$  and  $\text{C}_{10}\text{H}_{14}\text{O}^+$  and an especially large mass calibration perturbation of  $\pm 200$  ppm, to reflect the low confidence in the mass calibration. From these analyses we conclude that (i) the integrated area can be reconstructed from summed fitted peak intensities to within a few percent (excluding points with weak signals less than  $2 \text{ ions s}^{-1}$  where counting error is large); (ii) the fitted intensity of  $\text{As}_2^+$  is not sensitive to calibration imperfections, exhibiting  $\Delta_1 \sim 20\%$  with a 200 ppm offset; and (iii) the predicted imprecision on this intensity,  $\sigma_1$ , is also (coincidentally)  $\sim 20\%$ . Although this example presents a truly challenging peak-fitting scenario with limited signal, a large degree of peak overlap and an uncertain mass calibration, it can be confidently concluded that there is a non-negligible contribution to mass loading from the metal ion  $\text{As}_2^+$ . One may also draw conclusions based on the actual fitted peak intensities provided they hold true for changes of  $\pm 20\%$ .

Further analyses were conducted for other potential metal ions in the mine dataset, showing good evidence for the presence of the Zn isotopes (Fig. S25). A weak but non-zero signal was also found for  $\text{In}^+$  (Fig. S26). Other potential candidates showed either negligible signal or sensitivity analyses showed their fitted intensities to be unreliable (e.g. for  $\text{Cu}^+$ , Fig. S27).

### 4.7 Refinement of hydrocarbon-like organic aerosols (HOA)/oxygenated organic aerosols (OOA) constants

Previous studies have shown that the organic fraction can be typically separated into two main components: HOA and OOA. Based on previous AMS studies, Ng et al. (2011a) proposed a simple methodology for estimating the concentrations of OOA and HOA from the integrated signals at 44 and 57 Th, giving the relationship for HOA  $\sim 13.4 \times (C_{57} - a \times C_{44})$ , where  $C_x$  represents the integrated signal over the isobar peak at  $m/Q = X$ . The constant  $a$  was estimated as 0.1 and accounts for the predicted concentration of the interfering oxygenated ion  $\text{C}_3\text{H}_5\text{O}^+$  at 57 Th, where the majority of ion signal can be attributed to  $\text{C}_4\text{H}_7^+$ .

In ToF-ACSM these two ions are separated by  $X = 0.6$  Th at  $m/\Delta m = 450$  and are thus, with some degree of uncertainty, separable in the mass spectra. Thus a linear regression can be made of the fitted ion intensities of  $\text{CO}_2^+$  and  $\text{C}_3\text{H}_5\text{O}^+$  to calculate the constant  $a$  for the dataset under analysis, as shown for the SMEAR III dataset in Fig. S28. The derived slope for the SMEAR III data of 0.04 led to an increase in

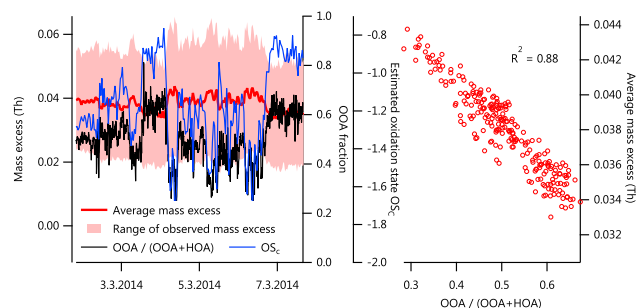


**Figure 15.** Time series (left) and regression (right) of the average mass excess and OOA fractions. Shown also the time series of the estimated carbon oxidation state from mass excess analysis.

estimated HOA concentrations of 6% with respect to using the default value of 0.1.

### 4.8 Oxidation state from analysis of mass excess

The limited mass resolving power of the ETOF-equipped ToF-ACSM precludes the calculation of the oxidation state (see Kroll et al., 2011) and O/C and H/C ratios using the elemental analysis approach commonly employed in HR-ToF-AMS analysis and detailed in Aiken et al. (2007) and Canagaratna et al. (2015). However, it was recently shown that molecular and bulk chemical information can be extracted from series of complex mass spectra with limited mass resolution using a method developed by Stark et al. (2015). They demonstrated using chemical ionisation data that the carbon oxidation state approximately follows the observed mass excess of the fitted ion peaks. Given that this principle of mass excess variation applies generally to all organic molecules irrespective of the ionisation technique, a similar mass excess analysis was thus applied to the SMEAR III data to investigate the aerosol oxidation state. Stark et al. (2015) used the higher mass resolving power of their data together with comprehensive ion lists to analyse the mass excess of all the fitted ions using the constrained peak-fitting methods described in Sect. 3. A mass resolving power of  $\sim 500$  precludes this approach, so instead the simpler bulk mass spectrum method also proposed by Stark et al. (2015) was employed. In this method, the average mass excess is calculated from the individual mass excesses of the mass spectral data points, weighted by their respective intensities. A mean average of the mass excess for the mass spectral data points for each isobaric MS peak between 41 and 100 Th, except those known to be influenced by inorganic ions such as  $\text{SO}^+$ , was generated by weighting to the observed signal level at each point. The range and weighted mean average of the mass excess values are plotted for a time series of a few days in Fig. 15. The OOA and HOA components were also calculated following methodology of Ng et al. (2011a) and the relative fraction of OOA is also shown. The average mass excess exhibits a clear anti-correlation with the OOA fraction

**Table 4.** Summary of ions of interest, their isobaric interferences and recommended magnitudes for calibration sensitivity analyses for various aerosol species measurable with the ToF-ACSM.

Species	Nominal mass (Th)	Ion of interest	Principal interference(s)	Closest peak separation $X$	Sensitivity (ppm)	Maximum intensity ratio of influencing peak / peak of interest $\times$ to achieve 25 % precision
Nitrate	30	NO <sup>+</sup>	CH <sub>2</sub> O <sup>+</sup> , C <sub>2</sub> H <sub>6</sub> <sup>+</sup>	0.3	10–20	3
Nitrate	46	NO <sub>2</sub> <sup>+</sup>	CH <sub>2</sub> O <sub>2</sub> <sup>+</sup> , C <sub>2</sub> H <sub>6</sub> O <sup>+</sup>	0.3	15–20	3
Sulfate	48	SO <sup>+</sup>	C <sub>4</sub> <sup>+</sup> , CH <sub>4</sub> O <sub>2</sub> <sup>+</sup>	0.5	20	5
Sulfate	64	SO <sub>2</sub> <sup>+</sup>	C <sub>5</sub> H <sub>4</sub> <sup>+</sup>	0.8	50	6
Sulfate	80	SO <sub>3</sub> <sup>+</sup>	C <sub>5</sub> H <sub>4</sub> O <sup>+</sup> , C <sub>6</sub> H <sub>8</sub> <sup>+</sup>	0.7	50–100	6
Sulfate	81	HSO <sub>3</sub> <sup>+</sup>	C <sub>5</sub> H <sub>5</sub> O <sup>+</sup> , C <sub>6</sub> H <sub>9</sub> <sup>+</sup>	0.7	50–100	6
Sulfate	98	H <sub>2</sub> SO <sub>4</sub> <sup>+</sup>	C <sub>5</sub> H <sub>6</sub> O <sub>2</sub> <sup>+</sup> , C <sub>6</sub> H <sub>10</sub> O <sup>+</sup> , C <sub>7</sub> H <sub>14</sub> <sup>+</sup>	0.6	50–100	5
Sodium Chl.	58	Na <sup>35</sup> Cl <sup>+</sup>	C <sub>2</sub> H <sub>2</sub> O <sub>2</sub> <sup>+</sup> , C <sub>3</sub> H <sub>6</sub> O <sup>+</sup> , C <sub>4</sub> H <sub>10</sub> <sup>+</sup>	0.6	50	5
Sodium Chl.	60	Na <sup>37</sup> Cl <sup>+</sup>	C <sub>5</sub> <sup>+</sup> , C <sub>2</sub> H <sub>4</sub> O <sub>2</sub> <sup>+</sup> , C <sub>3</sub> H <sub>8</sub> O <sup>+</sup>	0.6	50	5
Sodium Chl.	126	Fe <sup>35</sup> Cl <sub>2</sub> <sup>+</sup>	C <sub>5</sub> H <sub>2</sub> O <sub>4</sub> <sup>+</sup> , C <sub>6</sub> H <sub>6</sub> O <sub>3</sub> <sup>+</sup> , C <sub>10</sub> H <sub>6</sub> <sup>+</sup>	0.8	100	6
Sodium Chl.	128	Fe <sup>37</sup> Cl <sup>35</sup> Cl <sup>+</sup>	C <sub>4</sub> O <sub>5</sub> <sup>+</sup> , C <sub>6</sub> H <sub>8</sub> O <sub>3</sub> <sup>+</sup> , C <sub>10</sub> H <sub>8</sub> <sup>+</sup>	0.8	100	6
MSA	65	HSO <sub>2</sub> <sup>+</sup>	C <sub>4</sub> HO <sup>+</sup> , C <sub>5</sub> H <sub>5</sub> <sup>+</sup>	0.3	50	4
MSA	78	CH <sub>2</sub> SO <sub>2</sub>	C <sub>5</sub> H <sub>2</sub> O <sup>+</sup> , C <sub>6</sub> H <sub>6</sub> <sup>+</sup>	0.3	50–100	4
MSA	79	CH <sub>3</sub> SO <sub>2</sub>	C <sub>5</sub> H <sub>3</sub> O <sup>+</sup> , C <sub>6</sub> H <sub>7</sub> <sup>+</sup>	0.3	50–100	4

with  $R^2 = 0.88$ , supporting the validity of the method for the assessment of aerosol oxidation.

The parameterisation proposed by Stark et al. (2015, see also in the Supplement) is used to estimate the bulk aerosol carbon oxidation state, OS<sub>C</sub>, from the mass excess values. The values lie between  $-1.6$  and  $-0.8$  and are consistent with HOA and “fresh” semi-volatile OOA (SV-OOA) (Kroll et al., 2011), as expected for an urban measurement location.

To support the validity of this method, the estimated oxidation state value was also analogously calculated from spectra generated for a range of organic standards using the data presented in Canagaratna et al. (2015). For each compound, synthetic ETOF spectra were created by convolving a typical ETOF transfer function with the list of fitted ions and their intensities from the HR-ToF-AMS peak-fitting results of Canagaratna et al. (2015). The estimated oxidation state calculated from these spectra is compared to the values calculated from the elemental composition in Fig. 16, exhibiting  $R^2 = 0.77$  and quantitative agreement to within 1.5 %. This indicates that ETOF mass spectra have sufficient mass resolving power for the successful quantitative application of this method.

The parameterisations of Aiken et al. (2008) and Canagaratna et al. (2015) are often utilised to estimate the aerosol O:C ratio from integrated nominal-mass data based on the ratio of the integrated organic signal at 44 Th to that of all organic peaks, known as  $f_{44}$ . However, discrepancies were noted in  $f_{44}$  between instruments during the recent ACTRIS ACSM intercomparison exercise (Crenn et al., 2015; Fröhlich et al., 2015). As the mass excess parameterisation for oxidation state estimation described here depends on many

more signals than just CO<sub>2</sub><sup>+</sup>, it could potentially be a more reproducible method for investigating aerosol oxidation; this reproducibility across instruments should be a focus of future intercomparison exercises. Variability in mass calibration is a potential source of bias; however, an extrapolated calibration using just the air peaks would be sufficient to capture the mass range considered here (under 100 Th) and could be systematically applied. We note also that application of a 50 ppm mass calibration bias introduces a corresponding bias in OS<sub>C</sub> of only  $\sim 0.2$ .

## 5 Conclusions

The separation of isobaric ions using constrained peak fitting in data from the recently developed time-of-flight aerosol chemical speciation monitor (ToF-ACSM) was investigated. Details of the constrained peak-fitting methodology were given and a thorough discussion on mass calibration techniques presented. From the peak-fitting results, the following was demonstrated for the atmospherically relevant example datasets.

- The intensities of the ammonium ions NH<sub>x</sub><sup>+</sup> could not be reliably deconvolved from those of their relatively large isobaric interferences.
- The intensities of the nitrate ions NO<sup>+</sup> and NO<sub>2</sub><sup>+</sup> could be reliably deconvolved from their heavily overlapping isobaric organic interferences owing to high confidence in the mass calibration in the appropriate regions of the mass spectrum ( $\Delta_I < 10\%$ ,  $\sigma_I < 10\%$ ).



## References

- Aiken, A. C., DeCarlo, P. F., and Jimenez, J. L.: Elemental Analysis of Organic Species with Electron Ionization High-Resolution Mass Spectrometry, *Anal. Chem.*, 79, 8350–8358, doi:10.1021/ac071150w, 2007.
- Aiken, A. C., DeCarlo, P. F., Kroll, J. H., Worsnop, D. R., Huffman, J. A., Docherty, K., Ulbrich, I. M., Mohr, C., Kimmel, J. R., Sueper, D., Sun, Y., Zhang, Q., Trimborn, A., Northway, M., Ziemann, P. J., Canagaratna, M. R., Onasch, T. B., Alfarra, M. R., Prevot, A. S. H., Dommen, J., Duplissy, J., Metzger, A., Baltensperger, U., and Jiménez, J. L.: O/C and OM/OC Ratios of Primary, Secondary, and Ambient Organic Aerosols with a High-Resolution Time-of-Flight Aerosol Mass Spectrometer, *Environ. Sci. Technol.*, 42, 4478–4485, 2008.
- Allan, J. D., Coe, H., Bower, K. N., Alfarra, M. R., Delia, A. E., Jimenez, J. L., Middlebrook, A. M., Drewnick, F., Onasch, T. B., Canagaratna, M. R., Jayne, J. T., and Worsnop, D. R.: Technical Note: Extraction of Chemically Resolved Mass Spectra from Aerodyne Aerosol Mass Spectrometer Data, *J. Aerosol Sci.*, 35, 909–922, 2004.
- Aurela, M., Saarikoski, S., Niemi, J. V., Canonaco, F., Prevot, A. S. H., Frey, A., Carbone, S., Kousa, A., and Hillamo, R.: Chemical and Source Characterization of Submicron Particles at Residential and Traffic Sites in the Helsinki Metropolitan Area, Finland, *Aerosol Air Qual. Res.*, 15, 1213–1226, doi:10.4209/aaqr.2014.11.0279, 2015.
- Canagaratna, M. R., Jimenez, J. L., Kroll, J. H., Chen, Q., Kessler, S. H., Massoli, P., Hildebrandt Ruiz, L., Fortner, E., Williams, L. R., Wilson, K. R., Surratt, J. D., Donahue, N. M., Jayne, J. T., and Worsnop, D. R.: Elemental ratio measurements of organic compounds using aerosol mass spectrometry: characterization, improved calibration, and implications, *Atmos. Chem. Phys.*, 15, 253–272, doi:10.5194/acp-15-253-2015, 2015.
- Cappellin, L., Biasioli, F., Granitto, P. M., Schuhfried, E., Soukoulis, C., Costa, F., Mark, T. D., and Gasperi, F.: On data analysis in PTR-TOF-MS: From raw spectra to data mining, *Sensor Actuat. B-Chem.*, 155, 183–190, doi:10.1016/j.snb.2010.11.044, 2011.
- Charlson, R. J., Lovelock, J. E., Andreae, M. O., and Warren, S. G.: Oceanic phytoplankton, atmospheric sulphur, cloud albedo and climate, *Nature*, 326, 655–661, 1987.
- Corbin, J. C., Othman, A., Allan, J. D., Worsnop, D. R., Haskins, J. D., Sierau, B., Lohmann, U., and Mensah, A. A.: Peak-fitting and integration imprecision in the Aerodyne aerosol mass spectrometer: effects of mass accuracy on location-constrained fits, *Atmos. Meas. Tech.*, 8, 4615–4636, doi:10.5194/amt-8-4615-2015, 2015.
- Crenn, V., Sciare, J., Croteau, P. L., Verlhac, S., Fröhlich, R., Belis, C. A., Aas, W., Äijälä, M., Alastuey, A., Artiñano, B., Bainsée, D., Bonnaire, N., Bressi, M., Canagaratna, M., Canonaco, F., Carbone, C., Cavalli, F., Coz, E., Cubison, M. J., Esser-Gietl, J. K., Green, D. C., Gros, V., Heikkinen, L., Herrmann, H., Lunder, C., Minguillón, M. C., Mocnik, G., O'Dowd, C. D., Ovadnevaite, J., Petit, J.-E., Petralia, E., Poulain, L., Priestman, M., Riffault, V., Ripoll, A., Sarda-Estève, R., Slowik, J. G., Setyan, A., Wiedensohler, A., Baltensperger, U., Prévôt, A. S. H., Jayne, J. T., and Favez, O.: ACTRIS ACSM intercomparison – Part 1: Reproducibility of concentration and fragment results from 13 individual Quadrupole Aerosol Chemical Speciation Monitors (Q-ACSM) and consistency with co-located instruments, *Atmos. Meas. Tech.*, 8, 5063–5087, doi:10.5194/amt-8-5063-2015, 2015.
- Csavina, J., Field, J., Taylor, M. P., Gao, S., Landázuri, A., Betterton, E. A., and Sáez, A. E.: A review on the importance of metals and metalloids in atmospheric dust and aerosol from mining operations, *Sci. Total Environ.*, 433, 58–73, 2012.
- Cubison, M. J. and Jimenez, J. L.: Statistical precision of the intensities retrieved from constrained fitting of overlapping peaks in high-resolution mass spectra, *Atmos. Meas. Tech.*, 8, 2333–2345, doi:10.5194/amt-8-2333-2015, 2015.
- DeCarlo, P. F., Kimmel, J. R., Trimborn, A., Northway, M. J., Jayne, J. T., Aiken, A. C., Gonin, M., Fuhrer, K., Horvath, T., Docherty, K., Worsnop, D. R., and Jimenez, J. L.: Field-Deployable, High-Resolution, Time-of-Flight Aerosol Mass Spectrometer, *Anal. Chem.*, 78, 8281–8289, 2006.
- Draxler, R. R. and Rolph, G. D.: HYSPLIT (HYbrid Single-Particle Lagrangian Integrated Trajectory) Model, NOAA Air Resources Laboratory, Silver Spring, MD, available at: <http://ready.arl.noaa.gov/HYSPLIT.php>, 2013.
- Drewnick, F., Hings, S. S., DeCarlo, P., Jayne, J. T., Gonin, M., Fuhrer, K., Weimer, S., Jimenez, J. L., Demerjian, K. L., Borrmann, S., and Worsnop, D. R.: A New Time-of-Flight Aerosol Mass Spectrometer (TOF-AMS) – Instrument Description and First Field Deployment, *Aer. Sci. Tech.*, 39, 637–658, 2005.
- Drewnick, F., Diesch, J.-M., Faber, P., and Borrmann, S.: Aerosol mass spectrometry: particle-vaporizer interactions and their consequences for the measurements, *Atmos. Meas. Tech.*, 8, 3811–3830, doi:10.5194/amt-8-3811-2015, 2015.
- Fröhlich, R., Cubison, M. J., Slowik, J. G., Bukowiecki, N., Prévôt, A. S. H., Baltensperger, U., Schneider, J., Kimmel, J. R., Gonin, M., Rohner, U., Worsnop, D. R., and Jayne, J. T.: The ToF-ACSM: a portable aerosol chemical speciation monitor with TOFMS detection, *Atmos. Meas. Tech.*, 6, 3225–3241, doi:10.5194/amt-6-3225-2013, 2013.
- Fröhlich, R., Crenn, V., Setyan, A., Belis, C. A., Canonaco, F., Favez, O., Riffault, V., Slowik, J. G., Aas, W., Äijälä, M., Alastuey, A., Artiñano, B., Bonnaire, N., Bozzetti, C., Bressi, M., Carbone, C., Coz, E., Croteau, P. L., Cubison, M. J., Esser-Gietl, J. K., Green, D. C., Gros, V., Heikkinen, L., Herrmann, H., Jayne, J. T., Lunder, C. R., Minguillón, M. C., Mocnik, G., O'Dowd, C. D., Ovadnevaite, J., Petralia, E., Poulain, L., Priestman, M., Ripoll, A., Sarda-Estève, R., Wiedensohler, A., Baltensperger, U., Sciare, J., and Prévôt, A. S. H.: ACTRIS ACSM intercomparison – Part 2: Intercomparison of ME-2 organic source apportionment results from 15 individual, co-located aerosol mass spectrometers, *Atmos. Meas. Tech.*, 8, 2555–2576, doi:10.5194/amt-8-2555-2015, 2015.
- Gondwe, M., Krol, M., Gieskes, W., Klaassen, W., and de Baar, H.: The contribution of ocean-leaving DMS to the global atmospheric burdens of DMS, MSA, SO<sub>2</sub>, and NSS SO<sub>4</sub>, *Global Biogeochem. Cy.*, 17, 1056, doi:10.1029/2002GB001937, 2003.
- IPCC: Climate Change 2013: The Physical Science Basis, Contribution of Working Group I to the Fifth Assessment Report of the Intergovernmental Panel on Climate Change, edited by: Stocker, T. F., Qin, D., Plattner, G.-K., Tignor, M., Allen, S. K., Boschung, J., Nauels, A., Xia, Y., Bex, V., and Midgley P. M., Cambridge University Press, Cambridge, United Kingdom and New York, NY, USA, 1535 pp., 2013.

- Jayne, J. T., Leard, D. C., Zhang, X., Davidovits, P., Smith, K. A., Kolb, C. E., and Worsnop, D. R.: Development of aerosol mass Spectrometer for Size and Composition Analysis of Submicron Particle, *Aerosol Sci. Tech.*, 33, 49–70, 2000.
- Jimenez, J. L., Jayne, J. T., Shi, Q., Kolb, C. E., Worsnop, D. R., Yourshaw, I., Seinfeld, J. H., Flagan, R. C., Zhang, X., Smith, K. A., Morris, J., and Davidovits, P.: Ambient Aerosol Sampling with an Aerosol Mass Spectrometer, *J. Geophys. Res.-Atmos.*, 108, 8425, doi:10.1029/2001JD001213, 2003.
- Junninen, H., Ehn, M., Petäjä, T., Luosujärvi, L., Kotiaho, T., Koskiainen, R., Rohner, U., Gonin, M., Fuhrer, K., Kulmala, M., and Worsnop, D. R.: A high-resolution mass spectrometer to measure atmospheric ion composition, *Atmos. Meas. Tech.*, 3, 1039–1053, doi:10.5194/amt-3-1039-2010, 2010.
- Järvi, L., Hannuniemi, H., Hussein, T., Junninen, H., Aalto, P. P., Hillamo, R., Mäkela, T., Keronen, P., Siivola, E., Vesala, T., and Kulmala, M.: The urban measurement station SMEAR III: Continuous monitoring of air pollution and surface-atmosphere interactions in Helsinki, Finland, *Boreal Environ. Res.*, 14, 86–109, 2009.
- Kendrick, E.: A mass scale based on  $\text{CH}_2 = 14.0000$  for high resolution mass spectrometry of organic compounds, *Anal. Chem.*, 35, 2146–2154, 1963.
- Kimmel, J. R., Farmer, D. K., Cubison, M. J., Sueper, D., Tanner, C., Nemitz, E., Worsnop, D. R., Gonin, M., and Jimenez, J. L.: Real-time Aerosol Mass Spectrometry with Millisecond Resolution, *Int. J. Mass Spec.*, 303, 15–26, doi:10.1016/j.ijms.2010.12.004, 2011.
- Kroll, J. H., Donahue, N. M., Jimenez, J. L., Kessler, S. H., Canagaratna, M. R., Wilson, K. R., Altieri, K. E., Mazzoleni, L. R., Wozniak, A. S., Bluhm, H., Mysak, E. R., Smith, J. D., Kolb, C. E., and Worsnop, D. R.: Carbon Oxidation State as a Metric for Describing the Chemistry of Atmospheric Organic Aerosol, *Nat. Chem.*, 3, 133–139, doi:10.1038/NCHEM.948, 2011.
- Korhonen, H., Carslaw, K. S., Spracklen, D. V., Mann, G. W., and Woodhouse, M. T.: Influence of oceanic dimethyl sulfide emissions on cloud condensation nuclei concentrations and seasonality over the remote Southern Hemisphere oceans: A global model study, *J. Geophys. Res.*, 113, D15204, doi:10.1029/2007jd009718, 2008.
- Lawson, C. L. and Hanson, R. J.: *Solving Least Squares Problems*, SIAM, 1995.
- Meija, J. and Caruso, J. A.: Deconvolution of isobaric interferences in mass spectra, *J. Am. Soc. Mass Spectrom.*, 15, 654–658, 2004.
- Müller, M., Mikoviny, T., Jud, W., D’Anna, B., and Wisthaler, A.: A new software tool for the analysis of high resolution PTR-TOF mass spectra, *Chemometr. Intell. Lab.*, 127, 158–165, 2013.
- Ng, N. L., Canagaratna, M. R., Jimenez, J. L., Zhang, Q., Ulbrich, I. M., and Worsnop, D. R.: Real-time methods for estimating organic component mass concentrations from aerosol mass spectrometer data, *Environ. Sci. Technol.*, 45, 910–916, 2011a.
- Ng, N. L., Herndon, S. C., Trimborn, A., Canagaratna, M. R., Croteau, P. L., Onasch, T. B., Sueper, D., Worsnop, D. R., Zhang, Q., Sun, Y. L., and Jayne, J. T.: An Aerosol Chemical Speciation Monitor (ACSM) for Routine Monitoring of the Composition and Mass Concentrations of Ambient Aerosol, *Aer. Sci. Tech.*, 45, 780–794, doi:10.1080/02786826.2011.560211, 2011b.
- Ortega, A. M., Day, D. A., Cubison, M. J., Brune, W. H., Bon, D., de Gouw, J. A., and Jimenez, J. L.: Secondary organic aerosol formation and primary organic aerosol oxidation from biomass burning smoke in a flow reactor during FLAME-3, *Atmos. Chem. Phys.*, 13, 13799–13851, 2013.
- Ovadnevaite, J., Ceburnis, D., Canagaratna, M., Berresheim, H., Bialek, J., Martucci, G., Worsnop, D. R., and O’Dowd, C.: On the effect of wind speed on submicron sea salt mass concentrations and source fluxes, *J. Geophys. Res.-Atmos.*, 117, D16201, doi:10.1029/2011jd017379, 2012.
- Phinney, L., Leaitch, W., Lohmann, U., Boudries, H., Worsnop, D. R., Jayne, J. T., Toom-Saunty, D., Wadleigh, M., Sharma, S., and Shantz, N.: Characterization of the aerosol over the sub-arctic north east Pacific Ocean, *Deep-Sea Res. Pt. II*, 53, 2410–2433, doi:10.1016/j.dsr2.2006.05.044, 2006.
- Pope, C. A. and Dockery, D. W.: Health Effects of Fine Particulate Air Pollution: Lines that Connect, *J. Air Waste Manage. Assoc.*, 56, 709–742, 2006.
- Salcedo, D., Laskin, A., Shutthanandan, V., and Jimenez, J. L.: Feasibility of the Detection of Trace Elements in Particulate Matter Using Online High-Resolution Aerosol Mass Spectrometry, *Aer. Sci. Tech.*, 46, 1187–1200, doi:10.1080/02786826.2012.701354, 2012.
- Schmale, J., Schneider, J., Nemitz, E., Tang, Y. S., Dragosits, U., Blackall, T. D., Trathan, P. N., Phillips, G. J., Sutton, M., and Braban, C. F.: Sub-Antarctic marine aerosol: dominant contributions from biogenic sources, *Atmos. Chem. Phys.*, 13, 8669–8694, doi:10.5194/acp-13-8669-2013, 2013.
- Stark, H., Yatavelli, R. N. L., Thompson, S. L., Kimmel, J. R., Cubison, M. J., Chhabra, P. J., Canagaratna, M. R., Jayne, J. T., Worsnop, D. R., and Jimenez, J. L.: Methods to extract molecular and bulk chemical information from series of complex mass spectra with limited mass resolution, *Int. J. Mass Spec.*, 289, 26–38, doi:10.1016/j.ijms.2015.08.011, 2015.
- Sueper, D.: ToF-AMS High Resolution Analysis Software – Pika, available at: <http://cires.colorado.edu/jjimenez-group/ToFAMSResources/ToFSoftware/PikaInfo>, 2008.
- Weller, R., Minikin, A., Wagenbach, D., and Dreiling, V.: Characterization of the inter-annual, seasonal, and diurnal variations of condensation particle concentrations at Neumayer, Antarctica, *Atmos. Chem. Phys.*, 11, 13243–13257, doi:10.5194/acp-11-13243-2011, 2011.
- Weller, R., Schmidt, K., Teinilä, K., and Hillamo, R.: Natural new particle formation at the coastal Antarctic site Neumayer, *Atmos. Chem. Phys.*, 15, 11399–11410, doi:10.5194/acp-15-11399-2015, 2015.
- Yin, F., Grosjean, D., Flagan, R. C., and Seinfeld, J. H.: Photooxidation of dimethyl sulfide and dimethyl disulfide: Mechanisms evaluation, *J. Atmos. Chem.*, 11, 365–399, 1990.
- Zahradník, P. and Vlček M.: Fast Analytical Design Algorithms for FIR Notch Filters, *IEEE T. Circuits Syst.*, 51, 608–623, 2004.